

Mode-1 internal tides in the western North Atlantic Ocean

Brian D. Dushaw

*Applied Physics Laboratory,
College of Ocean and Fishery Sciences,
University of Washington, Seattle, Washington*

Submitted 23 February 2005; Revised 4 October 2005; Revised November 17, 2005

Corresponding author address: Dr. Brian Dushaw, Applied Physics Laboratory, University of Washington, 1013 N.E. 40th Street, Seattle, WA 98105-6698

21 November 2005

ABSTRACT

Mode-1 internal tides were observed the western North Atlantic using an ocean acoustic tomography array deployed in 1991–1992 centered on 25°N, 66°W.. The pentagonal array, 700-km across, acted as an antenna for mode-1 internal-tides. Coherent internal-tide waves with $O(1\text{ m})$ displacements were observed traveling in several directions. Although the internal tides of the region were relatively quiescent, they were essentially phase locked over the 200–300 day data record lengths. Both semidiurnal and diurnal internal waves were detected, with wavenumbers consistent with those calculated from hydrographic data. The M_2 internal-tide energy flux was estimated to be about 70 W m^{-1} , suggesting that mode-1 waves radiate 0.2 GW of energy, with large uncertainty, from the Caribbean island chain at this frequency. A global tidal model (TPXO 5) suggested that 1–2 GW is lost from the M_2 barotropic tide over this region, but the precise value was uncertain because the complicated topography makes the calculation problematic. In any case, significant conversion of barotropic to baroclinic tidal energy does not occur in the western North Atlantic basin. It is apparent, however, that mode-1 internal tides have very weak decay and retain their coherence over great distances, so that ocean basins may be filled up with such waves. Observed diurnal amplitudes were an order of magnitude larger than expected. The amplitude and phase variations of the K_1 and O_1 observed over the tomography array were consistent with the theoretical solutions for standing internal waves near their turning latitude. The energy densities of the resonant diurnal internal waves were roughly twice those of the barotropic tide at those frequencies.

Key Words: Internal waves; Internal tides; Baroclinic mode; Acoustic tomography; Western North Atlantic; 19–32N; 62–71W

1. Introduction

This paper describes observations of the low-mode internal tides in the western North Atlantic Ocean during the Acoustic Mid-Ocean Dynamics Experiment (AMODE). Acoustic tomography (Munk et al. 1995) and thermistors are used for these observations. The nature of the high-frequency variability (> 1 cpd) of travel times of long-range acoustic transmissions, including tidal variability, has been of concern since the 1970's (Clark and Kronengold 1974; Weinberg et al. 1974; Jobst and Dominijanni 1979; Dyson et al. 1976; Munk et al. 1981). Radiation of coherent, mode-1 internal tides from the Hawaiian Ridge into the central Pacific Ocean was first reported by Dushaw et al. (1995) using acoustic tomography, and the origin of this radiation was subsequently confirmed by Ray and Mitchum (1996) using altimetry. Bracher and Flatté (1997) described other measurements of internal tides in the central Pacific using long-range acoustics. A preliminary description of the diurnal internal tides observed during AMODE was given by Dushaw and Worcester (1998). Low-mode internal tides have been observed as coherent waves at many places in the world's oceans using TOPEX/Poseidon altimetry (Ray and Mitchum 1996, 1997; Kantha and Tierney 1997; Cummins et al. 2001; Ray and Cartwright 2001; Dushaw 2002). Both the acoustic and altimetric observations are consistent in the suggestion that the lowest-mode internal tide can propagate linearly as a coherent wave over distances of 1000–2000 km or more, though the acoustic observations make this case a little more strongly. The first hint of this property of low-mode internal waves was by Hendry (1977), who found that coherent internal tides traveled 700 km from the Blake Escarpment to the Mid-Ocean Dynamics Experiment (MODE) array (Fig. 1).

Although of interest in their own right, internal tides have received a great deal of attention in recent years for their possible role as a catalyst for the deep-ocean mixing that plays such an important role in the oceanic general circulation (Sjoberg and Stigebrandt 1992; Munk and Wunsch 1998). The generation of internal tides by interaction of

the barotropic tidal currents with topography is one way by which tidal energy may become available for mixing. The Hawaiian Ocean Mixing Experiment (HOME) was recently conducted to better quantify these issues (Pinkel et al. 2000). The present paper has little direct relevance to the mixing problem, however. Not only do the low-mode internal tides appear to have very weak dissipation, so that their energy is not readily available for mixing, but, as we will see, the energies of the internal tides observed during AMODE are relatively weak compared to internal tides in likely regions of intense tidal dissipation, e.g., Pinkel et al. (2000), Egbert and Ray (2000; 2001; 2003).

The 1991–1992 AMODE experiment is described in detail by the AMODE Group (1994); Dushaw et al. (1996, 1997), Dushaw and Worcester (1998), and Dushaw (2003); a short description of this experiment and its associated data will be given in section 2. Dushaw et al. (1997) critically compare the acoustically-derived barotropic tidal currents and relative vorticity to the TPXO.2 global tidal model of Egbert, et al. (1994). The harmonic constants for currents from the tidal model agreed to within 2% of the harmonic constants derived from the direct, acoustically-measured currents. Small, systematic differences between the measured and modeled currents were observed, and these were traced to dynamical errors in the tidal model resulting from assumptions about the scale of the modeling error. The results concerning the barotropic tide are relevant here because the baroclinic tide signals in the acoustic travel time data are almost as phase locked to the tidal frequencies as the barotropic signals. The baroclinic signals are subject to noise from internal-waves or incoherent elements of the baroclinic tide, so they are not quite as good as the barotropic signals.

Dushaw (2003) described the antenna properties of acoustic tomography arrays, with the AMODE array as an example, for observing internal-tide radiation. In brief, given an internal-tide field of arbitrary vertical mode and wavenumber content, tomography measures only the first baroclinic mode and only wavenumbers perpendicular to the

tomography path.

The AMODE array was located in about the same place as the MODE array (Fig. 1), so the internal tides described by Hendry (1977) likely passed through the AMODE array. The tomographic observation of internal tides gives a unique opportunity to understand the generation and propagation of a deterministic component of internal waves. The observed internal tides are assumed to be generated at the continental shelf surrounding the western North Atlantic basin. Recent numerical modeling of internal-tide generation at Hawaii and elsewhere (Kang et al. 2000; Merrifield et al. 2001; Cummins et al. 2001; Merrifield and Holloway 2002; Simmons et al. 2004; Arbic et al. 2004) supports this view of internal tide generation. The internal waves induced at sharp topographic features such as mid-ocean ridges or continental shelves propagate great distances into the oceanic interior.

In section 2, the tidal signals in the acoustic, thermistor and hydrographic data are described. In section 3, the semidiurnal harmonic constants for the internal-tide signals are shown to be consistent with several coherent waves traveling through the acoustic array from several directions, and the diurnal harmonic constants are introduced. The term "harmonic constant" is used with the tentative conclusion that mode-1 internal tides can be represented by such constants, much as the barotropic tides are. In section 4, the solutions for the meridional structure of internal waves with a no-flow southern boundary and a nearby northern turning latitude are given, and these solutions are compared to the measured diurnal harmonic constants. In section 5, the energetics of these internal tides are described and compared to the barotropic energies. In section 6, the conclusions are discussed.

2. The Acoustic Mid-Ocean Dynamics Experiment (AMODE)

AMODE consisted of a pentagonal array of 250-Hz transceiver moorings deployed to determine the ability of ocean acoustic tomography, together with moving ship tomography, to map and explore mesoscale dynamics (The AMODE Group 1994; Cornuelle and Worcester 1996). The 700-km diameter array was located mid-way between Bermuda and Puerto Rico (Figs. 1, 2, Table 1). The 15 acoustic paths of the array are of lengths 350, 410, or 660 km. The acoustic transmissions were reciprocal so that current and sound speed variability can be distinguished.

a. Acoustic data

The tomography array was deployed in March 1991, and reciprocal acoustic transmissions were obtained for 180–300 days, depending on instrument battery power. Transmissions occurred every three hours on every fourth day. During summer 1991, transmissions occurred every three hours continuously for a three week period during the Moving Ship Tomography experiment (The AMODE Group 1994; Cornuelle and Worcester 1996). Notation such as "path (1,2)" will be used to indicate the acoustic path from mooring 1 to mooring 2.

From 8–12 ray arrivals were resolved in the receptions on each acoustic path. These rays are typically refracted at their upper and lower turning points (Fig. 2). The presence of mode water strongly influences the structure of the ray paths. There is little sound speed gradient in this water, hence rays with upper turning points within the mode water (200–400 m) are not possible. Dushaw et al. (1995) showed that data obtained in the Pacific Ocean for the latest-arriving ray (the travel time of the "final cutoff" of the acoustic pulse) had a larger tidal signal than that from the deep-turning rays, because this ray sampled the ocean depths where the mode-1 temperature variations were largest. In the AMODE region, the sound channel axis lies well below the depth of mode-1

temperature maximum; the tidal signals from latest-arriving ray were almost identical to those from the deep-turning rays. The "final cutoff" travel times obtained during AMODE were also fairly noisy. Since the "final cutoff" data were noisy and offered no additional information, they were not used.

The ray travel times are corrected for the motion of the transceiver moorings using an acoustic tracking system around each transceiver mooring. With these corrections, and others for timing errors due to clock drift, the ray travel times have an instrumental uncertainty of about 1 msec. Internal wave variability introduces a travel time uncertainty of about 10 msec.

In order to separate the variations caused by currents from those caused by sound speed (or temperature), the difference and sum of the reciprocal-ray travel time data are formed. Tidal signals are evident in both the sum and the difference travel times. The internal tides are observed using the sum travel times (Fig. 3), which are sensitive to the isotach variations caused by vertical displacement. The sum travel times in this paper are high-pass filtered (> 1 cpd) by removing a daily average. This filter allows a more accurate tidal study; it does not adversely affect the tidal analysis (Dushaw et al. 1997). All subsequent references to the travel times are to these high-pass filtered sum travel times. The low-frequency travel time variations show mesoscale variability in both temperature and current which we are not concerned with here.

The eigenvalues of the equation for vertical modes (Appendix A gives the equations, notation and normalization for the modes) give the wavelengths and phase and group speeds of the waves, given the tidal constituent frequency (Table 3). Internal waves have a turning latitude where their frequency equals the inertial frequency; internal waves cannot freely propagate north of their turning latitude and waves approaching this latitude refract back towards the equator. AMODE was located just south of the turning latitudes for diurnal frequencies. The K_1 "wavelength" is around 480 km, but this "wavelength"

increases as the turning latitude is approached. These diurnal properties are described more fully in Section 4.

Dushaw et al. (1995) described the weighted least squares techniques used to solve for the amplitudes of the internal wave modes from the sum travel times and their identified ray paths. The integration of the internal tide modes over the acoustic ray paths determines the available resolution of the modes. The forward problem is

$$T_i^+(t) + T_i^-(t) \approx 2T_{0i} - 2 \int_{\Gamma_i} \frac{\sum_j A_j(t) \eta_j(z)}{c_0^2(\mathbf{x})} ds, \quad (1)$$

where T_i^+ and T_i^- are the reciprocal travel times for ray path Γ_i , $c_0(\mathbf{x})$ is a reference sound-speed field, $\eta_j(z)$ are the modes with amplitude $A_j(t)$, $\sum_j A_j(t) \eta_j(z) = \delta c(z, t)$ is the sound speed perturbation, ds is an increment of arc length, t is time (yearday), and $T_{0i} = \int_{\Gamma_i} \frac{ds}{c_0(\mathbf{x})}$. The integrals of the rays over the first mode all have about the same value,

while integrals over the higher modes are less than half as big and have both positive and negative values. The ray paths have similar sampling so they give limited vertical resolution, and the vertically-integrating nature of the data significantly cancels the effect of higher-order modes. For these reasons, the dominant signal in the data is caused by the lowest internal-tide mode. Five modes were used in the inversion to account for possible noise from the higher modes. A tidal analysis of the time series for mode amplitude then gives the harmonic constants of the internal tide signals; these results are discussed in the next section. There is no obvious signal of modes 2 or higher in these data, however. A tidal analysis of the mode-2 time series derived from the data from path (2,4) accounted for only 15% of the variance. All tidal phases in this paper are Greenwich epoch (Shureman 1958).

The estimated uncertainties of the harmonic constants require a comment. As described by Dushaw et al. (1995), weighted least squares are used to derive the harmonic constants. This approach allows for noise and some *a priori* weighting of the harmonic constants (e.g., the M_2 amplitude is obviously larger than the P_1 amplitude). However, the technique assumes that the noise is white, while the actual noise has an obvious tidal component, caused by higher-mode internal tides or a non-phase-locked component to the internal tides. As noted by Dushaw et al. (1995), the formal error bars from the harmonic analysis are therefore underestimated.

b. Thermistor data and spectra

Thermistor data were obtained on each of the six transceiver moorings at about 600, 700, and 950 m depths. The depths of the thermistors are located at depths near the maximum of the first temperature mode (Fig. 2). The first 6 temperature modes were fit to the thermistor data to extract time series of mode amplitudes. The three thermistors on each mooring obviously do not provide adequate resolution of the baroclinic modes. The first mode was assumed to be the dominant signal, and other modes were included in the fit to allow for noise.

The time series for the first mode were used to calculate frequency spectra of the internal wave field at a single point. The thermistor data, like nearly all thermistor data, have peaks in their spectra at both diurnal and semi-diurnal frequencies (Fig. 4). Spectra calculated using time series of temperature from single thermistors were similar to the mode-1 spectra, with a slightly elevated noise level, slightly weaker (2 dB) tidal peaks, and nearly identical widths of the tidal peaks. Even though these record lengths are longer than a year, the width of most of the spectral lines is determined by the finite record length, rather than by any instability in the internal-tide phase. (Noise in the thermistor records caused by mooring motion is reduced because the tomography moorings

are particularly stiff.) In this region at least, it seems that if the internal tide is a narrow-band process, its spectral width is smaller than may be determined by these data.

Other than tidal peaks in the spectra observed at the six moorings, no geographical pattern emerges from the spectra at either diurnal or semidiurnal frequencies. We might expect that the amplitudes for the diurnal internal tides from higher-latitude moorings, such as mooring 1, to be suppressed, since these moorings are near the turning latitude where the waves are nearly inertial, but this is not generally observed. It seems likely that contributions from higher-order modes to the observed temperatures cannot be adequately distinguished from the mode-1 signal. We will assume that the signal of mode-1 dominates in the thermistor data, but recognize that the derived time series of mode-1 amplitude may be significantly contaminated by higher modes.

The spectra of Fig. 4 show that the peaks for the semidiurnal and diurnal internal tides have surprisingly similar intensities. The K_1 line is only 5–7 dB weaker than the M_2 line in Fig. 4. The ratio of M_2 to K_1 barotropic current intensities, which might set the expected ratio for the internal tide intensities, is 15 or 23 dB, depending on whether the zonal or meridional currents are used for the calculation (Table 2).

c. Hydrographic data

Hydrographic sections were obtained during the deployment and recovery of the transceiver moorings. These data allow the vertical mode functions and their associated properties to be calculated somewhat more accurately than may be determined from climatology. During the three week deployment of the moorings in March 1991, 9 Conductivity Temperature Depth (CTD) casts were obtained to 2000 m, and 8 casts were obtained to near the ocean bottom. During the three week recovery in March 1992, 25 casts were obtained to around 2000 m depth, and 15 casts were obtained to around 5000 m depth.

The mode eigenvalues and eigenfunctions obtained depend on the stratification. The hydrographic data allow the variation of the mode properties over the region of the array to be assessed at the beginning and end of the experiment. Obviously, internal wave and internal-tide variability contaminate this assessment to some degree. Mode-1 internal tides have wavelengths of $O(150 \text{ km})$, and the small-scale noise in individual hydrographic casts would not actually influence low-mode properties. Values for the eigenvalues of the first mode obtained using data from the CTD casts had a mean and rms of $0.105 \pm 0.003 \text{ s m}^{-1}$ ($0.1065 \pm 0.0023 \text{ s m}^{-1}$ in 1991 and $0.1052 \pm 0.0034 \text{ s m}^{-1}$ in 1992). This 3% variation of the eigenvalues is small and likely to be an overestimate of the actual influence of stratification on mode properties. In any case, it is apparent that mode-1 properties are constant over the area of the array, and that mode-1 properties in March 1991 are identical to those in March 1992.

3. Harmonic constants of the internal tide

The tidal analyses of the time series of mode-1 amplitude obtained on the 15 paths of AMODE account for 33–77% of the variance of the mode-amplitude time series (Fig. 5, Table 4). Similar tidal analyses of the time series of mode amplitude derived from the thermistor data accounts for only 7–39% of the variance (Table 5). A unit amplitude is equivalent to about 1-m displacement at the depth of mode maximum at about 1500 m depth (Tables 4 and 5 use units of "cm" for convenience.) This displacement has a temperature signal of about $40 \text{ m}^\circ\text{C}$. These small signals are apparent in the tomography data because they have long spatial coherence lengths.

One concern has been that the internal tides may not actually be phase locked and that the harmonic analyses could be effective at fitting variability irrespective of what frequencies are used. As described by Dushaw and Worcester (1998), however, a tidal

analysis with "nearly" tidal frequencies shows that the signals observed by the long-range acoustics are phase locked, insofar as can be determined from the 180–300 day record lengths. A "tidal" analysis of these records with the frequencies shifted by $2\pi/(\text{record length})$ accounts for only 8% of the variance, or about the value expected from a time series of noise. Another test of internal-tide stability may be to divide the record lengths into 30-day subsections, say, and determine the variability of the harmonic constants derived from the subsections. This procedure was applied to these data, and the resulting phases and amplitudes for the harmonic constants usually varied slowly by 10-50% over the complete time series. The phases proved to have more stability than the amplitudes. The S_2 and K_1 harmonic constants had substantially more variability than the others. However, a "control" analysis using a simulated purely tidal signal, white noise, and identical sampling had similar results, both for the slow variations of amplitude and phase and for the greater variability of the S_2 and K_1 constants. The S_2 and K_1 constituents have periods of 12.0000 and 23.9345 hours, respectively, which are similar to the sampling intervals (i.e., eight 3-hourly measurements on every fourth day). While this procedure may suggest some slow variations in the harmonic constants over the record lengths, it is clear that the manner in which the irregular sampling affects the tidal analysis makes a precise measurement of those variations impossible. It is notable, however, that the sampling inherently makes the S_2 and K_1 constants a little more unstable than the others.

The semidiurnal phases obtained on the acoustic paths are consistent with the theoretically expected wavelength. For the semidiurnal frequency, the beam patterns of the line-segments of the array are quite narrow (Dushaw et al. 1995; Dushaw 2003), so the tidal variability observed on a particular path is caused by wave crests nearly aligned with that path, or wavenumbers perpendicular to that path. In the AMODE array, there are 5 pairs of paths that are parallel and separated by about 400 km (Fig. 1); each pair of paths is sensitive only to wavenumbers perpendicular to the paths. For both the M_2 and N_2

frequencies, the difference in phases observed on parallel paths is about 180° (Tables 6, 7). The values for the S_2 frequency do not have this property, although this constituent is weaker than N_2 in this region. If the S_2 signal is weaker than the noise, the harmonic constants for the S_2 constituent may not reliably show the coherent component of the internal tides. The 180° phase change on the parallel paths is consistent with wavelengths for which $(n + \frac{1}{2})\lambda = 400$ km, where $n = 0, \pm 1, \pm 2, \pm 3, \dots$ and λ is the wavelength of the radiation. Possible values for λ are therefore 800, 267, 160, 114, etc. km. The 160-km value for $n = 2$ is roughly the theoretically-expected wavelength for semidiurnal mode-1 waves. The wavelength cannot be uniquely determined from the data alone in this case; the ambiguity in the index n leads to side lobes in the wavenumber spectra estimated from these data, as described by Dushaw (2003). Wavenumber spectra calculated from these harmonic constants are consistent with the theoretically-expected wavelengths, for both semidiurnal and diurnal constituents (Dushaw and Worcester 1998; Dushaw 2003).

Hendry (1977) and Dushaw et al. (1995) used the "age" of the internal tide to calculate the distance the internal waves had travelled. The "aging" of the tide over a distance R is given by

$$(k_1 - k_2) R = (G_1 - G_2) - (G_1 - G_2)_0 \quad (2)$$

where the subscripts 1 and 2 refer to two of the tidal constituents, k is wavenumber, and G is tidal phase (e.g., Greenwich epoch). The subscript 0 refers to the initial phase difference between the two constituents. In the present case, the parallel paths can be used to obtain five independent estimates of the "aging" of the tide over the 400-km spacing of the paths. The M_2 and N_2 constituents can be used for this calculation. The left hand side of (2) is $(k_{M_2} - k_{N_2}) R = 23^\circ$ for $R = 400$ km. The right hand side of (2) has values for the five pairs of parallel paths (Tables 6 and 7): $-45 \pm 15^\circ$, $+11 \pm 25^\circ$, $+79 \pm 62^\circ$, $+21 \pm 19^\circ$, and $-6 \pm 12^\circ$. While these results are not sufficiently accurate to definitively test the

"aging" of the tide, the measured values agree with the expected 23° value within the rather large uncertainties. (Unfortunately, the M_2 and N_2 wavenumbers are too closely valued to give much "aging" over 400 km.)

Similarly, M_2 and N_2 phase differences may be related to the propagation from distant regions where internal tides originate. The N_2 phase for barotropic elevation leads the M_2 phase by about 20° throughout the western North Atlantic Basin (Table 2), which may be representative of the original phase difference between the internal tides at these frequencies (Hendry 1977). As an example, paths (4,5) and (1,3) would be most sensitive to radiation from the Blake Escarpment some 800 and 1200 km distant, respectively. The expected increase in phase lag between the M_2 and N_2 constituents over the 800 km from the Blake Escarpment to path (4,5) is 46° , while the phase increase to path (1,3) is 69° . Observed values for the "age" of the internal tides on these paths are 24° and 44° , respectively, with uncertainties of around 10° . The observed "age" of the internal tides reflects the approximate distance that these waves have travelled. Further, the differences between the M_2 and N_2 phases obtained on all paths (Fig. 6) are slightly greater than the barotropic phase difference, suggesting that the several waves observed on the various paths have traveled several hundred kilometers. The uncertainties make a precise estimate for the range of propagation impossible, however. Hendry (1977) made a similar calculation, using the results from MODE thermistor records and the phase differences between S_2 and M_2 constituents, to suggest that internal tides observed by the MODE array had an "age" consistent with the 700-km distance to the Blake Escarpment. For the acoustical results, the S_2 phases do not seem reliable enough for a meaningful calculation.

The harmonic constants derived on each acoustic path can be combined to form a single objective map of the internal tide for each constituent (Dushaw 2003). Figure 7 shows such a map for the M_2 constituent. Dushaw (2003) used an omnidirectional a

priori spectrum to calculate a similar tidal map, which resulted in standing wave solutions. Given the directional ambiguity inherent in the array, the objective map (i.e., least squares) assuming an omnidirectional spectrum gives solutions with opposite wavenumbers and equal amplitudes because $(A/2)^2 + (A/2)^2 < A^2$. For the map of Figure 7, a more reasonable assumption that the waves are propagating away from the nearby topography was used, and the *a priori* spectrum was selected for this purpose. The resulting map is obviously a complicated interference pattern resulting from the superposition of the various waves moving through the observing array. The M_2 amplitudes derived from the thermistor data on each mooring (Table 5) are considerably larger than those derived from the acoustic data for this reason. Given the extreme sensitivity of interference patterns to slight changes in phase of the underlying waves, it is little wonder that occasional past observations of internal tides by single thermistor or current meter moorings have had trouble detecting the coherent aspects of internal tides.

Diurnal amplitudes are large relative to the semidiurnal amplitudes (Table 4). Their amplitude is oftentimes as large as those for the semidiurnal amplitudes, yet from the barotropic tides the diurnals would be expected to be an order of magnitude smaller (Table 2; Figs. 1 and 8). The large diurnal amplitudes are apparent in the thermistor spectra as well. The next section demonstrates that the diurnal internal tides are in resonance - trapped between the Caribbean island arc and their turning latitudes at about 30°N.

The internal tides described here are not obvious in the observations by altimetry in this area (Ray and Mitchum 1997, Kantha and Tierney 1997), probably because the tidal variability shown in Fig. 7 does not offer the coherent, nearly monochromatic, waves that have been apparent in the along-track altimetry data at places such as the Hawaiian Ridge. The internal tides described here are also considerably weaker than those observed at other places, so their signal is not likely to be observable by altimetry. Diurnal internal tides, in particular, are not evident in the TOPEX/Poseidon altimeter data in

this region (R. Ray personal communication, 1999). The nominal resolution of TOPEX/Poseidon altimeter data is 3–4 cm, but the tidal harmonic constants derived from those data have uncertainty of 0.5–1.0 cm (R. Ray personal communication 2002). Dushaw (2002) found that an uncertainty of 0.4 cm was consistent with an objective map of sea-surface height for internal tides near Hawaii; there the tidal signals were of order 2.5 cm. The sea-surface height signals expected from the 1-m amplitude internal tides reported here are only of order 0.16 cm (Appendix A).

4. Resonant diurnal internal tides

The amplitude and phases observed for the diurnal internal tides are reasonably consistent with internal waves that are trapped between Puerto Rico and their turning latitude. Dushaw and Worcester (1998) gave a preliminary description of this phenomena. A more accurate, complete description is given here. The phase of the diurnal barotropic tide varies by only 10–20° along the north side of the Caribbean island arc (Fig. 8), so it is plausible that diurnal internal waves with coherent wave crests can be generated there.

The theory describing these internal waves is given by Wunsch and Gill (1976) (see also Philander (1978), and Hendershott (1973, 1981)), who found that peaks in the spectra of tropical Pacific tide gauge data at periods of a few days corresponded to low-order resonances of trapped, wind-forced internal waves. The general problem of equatorial waves near a zonal coastal boundary is described by Philander (1977). The waveforms for meridional current near the turning latitude are approximately Airy functions. For the K_1 frequency this latitude is 30.0°, while for the O_1 frequency this latitude is 27.6°. Dushaw and Worcester (1998) used the dispersion relation for these waves to solve for the approximate order of the Hermite function required to match the diurnal tidal frequencies. Zonal variations were much smaller than meridional variations, so zonal wavenumber was taken to be zero. The largest amplitudes are apparent on the zonal

acoustic paths. From Table 4, Paths (2,6), (2,4), and (4,6) have O_1 amplitudes 53, 64, 75, respectively, while paths (1,6), (1,3), and (3,6) have amplitudes 26, 17, 23, respectively. For the O_1 and K_1 frequencies, the orders of the Hermite functions were $m = 36$ and $m = 42$, respectively.

While these Airy-function solutions for the internal tides are suggestive of what is occurring across the AMODE array, this approach to a solution has a number of flaws: (1) The solutions are required to have zero flow at the southern boundary at some latitude to the north of Puerto Rico, while the solutions of Dushaw and Worcester (1998) employed no southern boundary. The boundary condition was somewhat respected only by chance for the K_1 frequency. (2) The region of interest (18–35°N) is far enough north and of such a large area that the beta-plane approximation may begin to break down. (3) Large orders such as 36 and 42 may not be entirely realistic. (4) There is no guarantee that with more accurate solutions, the eigenfrequencies will match those of the tides. (5) In calculating diurnal internal tide energy, Dushaw and Worcester (1998) used the ratio of potential to kinetic energy for free waves. In the next section, the energies are calculated using a more correct relation between potential and kinetic energy and more correct solutions for the wave shapes as a function of latitude.

Solutions for waves that resolve many of these issues are described next. The equations for the beta-plane approximation will be briefly reviewed, followed by equations and numerical solutions for the situation particular to the experiment domain.

For a constant depth D_n , the Laplace tidal equations can be used to derive the equation governing the variation of meridional current with latitude (Hendershott, 1981). Usually a beta plane approximation is used, so $f = \beta y$, where f is the inertial frequency, $\beta = df/dy$, and y is latitude. Separation of variables for meridional current is assumed,

$$v(x, y, z, t) \approx e^{ilx - i\omega t} V(y) F'(z) \quad (3)$$

and similarly for zonal and vertical currents and elevation. In this equation, l is zonal wavenumber and $F'(z)$ is the vertical mode for current, which is the derivative of the displacement mode. With these approximations, the equation governing $V(y)$ is,

$$\frac{d^2V(y)}{dy^2} + \left[\left(\frac{\omega^2}{gD_n} - l^2 - \frac{l\beta}{\omega} \right) - \frac{\beta^2}{gD_n} y^2 \right] V(y) = 0 \quad (4)$$

where g is gravitational acceleration. With boundary conditions $V = 0$ at $y = \pm \infty$, the solutions for this equation are Hermite functions. The equivalent depths, D_n , are derived from the equation for the vertical modes as described in Appendix A. The dispersion relation is

$$\left(\frac{\omega^2}{gD_n} - l^2 - \frac{l\beta}{\omega} \right) = (2m+1) \frac{\beta}{\sqrt{gD_n}} \quad (5)$$

More accurate solutions than these can be found numerically such that both the boundary conditions and the variation of the inertial frequency with latitude are taken into account. The difference between the beta-plane and more accurate solutions is small, but noticeable. Avoiding the beta-plane approximation (here taken to mean $f(y) \approx f_0 + \beta y$), but retaining the Cartesian approximation, (4) becomes

$$\frac{d^2V(y)}{dy^2} + \left(\frac{\omega^2}{gD_n} - l^2 - \frac{l}{\omega} \frac{df}{dy} - \frac{f^2(y)}{gD_n} \right) V(y) = 0 \quad (6)$$

with boundary conditions, $V = 0$ at the southern boundary and decaying to zero north of that boundary.

The solutions of the equation above are readily obtained using Runge-Kutta integration techniques (Abramowitz and Stegun, 1965). The differential equation is integrated for a sequence of frequency values (i.e., shooting); the eigenfunctions are those for which the solutions go to zero at ∞ . As discussed above, zonal wavenumber is taken to be zero. Of the eigenfrequencies found, modes 3 and 5 most nearly correspond to the O_1 and K_1 frequencies, respectively (Fig. 9). Conveniently, the shapes of these modes are similar to the mode solutions of order 36 and 42 found using the beta-plane approximation (Fig. 10). Since tomography measures the vertical displacement from these waves, the displacement modes (dV/dy) are also shown in Fig. 10 together with the latitudes of the tomography moorings.

The latitude of the southern boundary is chosen to give frequencies that most closely match the tidal frequencies. Varying the latitude of the southern boundary by even as much as a half degree, expands or contracts the eigenfunctions to fix the zero current at that latitude and substantially changes the eigenfrequencies. The region just to the north of Puerto Rico features a trench 8000 m deep, together with a scattering of islands to the northwest. These complications make the precise latitude of no meridional flow uncertain. It may be that the different frequencies have slightly different southern boundaries, depending on how the resonating waves are interacting with the trench, Puerto Rico, and islands. The latitude might be taken as something of a free parameter that can be used to adjust the solutions obtained. The solutions described below were obtained for a southern boundary at 19.5°N , which roughly corresponds to the latitude of the trench. The solutions also depend on the precise value used for $\lambda_1 = 1/gD_1$, and the turning latitude of the waves may depend on whether there is any zonal component to the wave. Because of these issues, these calculations must be taken as just a plausible description of

the meridional structure of the waves. It is encouraging that the spacing of the O_1 and K_1 frequencies roughly corresponds to the spacing of the eigenfrequencies, however.

These solutions to the variation of these waves with latitude compare reasonably well with the measured harmonic constants for the diurnal internal tides. Dushaw and Worcester (1998) qualitatively compared the diurnal harmonic constants derived from the acoustic (Table 5) and thermistor (Table 6) data to the approximate Airy function solutions for the internal waves near their turning latitude. Next, this preliminary comparison is extended by fitting the numerical solutions for these internal wave modes (these meridional modes are not to be confused with the vertical modes) to the harmonic constants. The quantitative fit can be expected to work reasonably well, given the initial favorable comparison: "For the K_1 frequency, the paths (2,4), (2,6), and (4,6) all lie along a trough of the predicted displacement, and the amplitudes (94, 101, and 76 cm) and phases (252, 262, and 282°) associated with these paths are consistent with the predicted wave" (Fig. 11; Dushaw and Worcester 1998).

For each constituent, the fit of the displacement mode to the data uses only two parameters, the amplitude and phase, to account for the 30 harmonic constants measured on the acoustic paths (an amplitude and a phase from each of the 15 acoustic paths). With the modes normalized to have a maximum value of 1, the fit gives an amplitude and phase for the K_1 mode of 134 cm, 85°, and an amplitude and phase for the O_1 mode of 89 cm, 325°. These solutions are compared to the data in Figure 12. The phases for both constituents are most strikingly consistent with a standing wave. The phases are roughly in two groups separated by 180°, as expected for a standing wave. Frequently, the mismatch between modeled and measured phase is by 180°, suggesting that the solutions for the displacement modes may not be quite right. For several of the acoustic paths, a minor shift in the location of the zero crossing of a mode results in a phase change of 180°, if that shift changes whether a crest or trough of the wave dominates in the path integral.

The K_1 meridional current just north of Puerto Rico has an amplitude of about 0.5 mms^{-1} and a phase of about 40° . The K_1 meridional mode used for this fit is positive near Puerto Rico (Fig. 10). Therefore, as previously reported by Dushaw and Worcester (1998), the time of maximum positive displacement of the K_1 internal tide just north of Puerto Rico (phase 85°) roughly corresponds to the maximum offshore (northward, phase 40°) flow of the barotropic current. This result appears to be inconsistent with the expected generating mechanism for internal tides, where onshore flow would cause an uplifting of isopycnals; the author cannot suggest an explanation.

The amplitudes for the K_1 constituent are suggestive of the standing wave model for the zonal paths (zonal paths have 0° azimuthal angle), but values for many of the meridional paths (e.g., near -80° azimuthal angle) are rather larger than expected from the model (Fig. 12). The large values from the meridional paths are not consistent with a zonally-independent standing wave, and suggest a zonal component to the waves. Spectra calculated from the K_1 harmonic constants (Dushaw and Worcester 1998; Dushaw 2003) do suggest that these diurnal waves are more complicated than a simple standing wave. One possible explanation may be that a mismatch between the K_1 tidal frequency and resonant frequency has caused a number of modes with frequencies adjacent to the K_1 frequency to be excited. Alternatively, the topography along the island chain constituting the southern boundary for these waves is complicated to the west, perhaps pushing the zero-meridional flow boundary as far north as $22\text{--}23^\circ\text{N}$ in some places, which would certainly affect the mode solutions. Another possibility is that diurnal internal waves propagating into this region from the equatorial Atlantic may "accumulate" as they interact with the Caribbean island chain, and so behave as a resonance (R. Pinkel personal communication 1999). This suggestion presents a view of these internal tides that would be difficult to model. The amplitudes for the O_1 constituent are remarkably consistent with the standing wave solution, however.

5. The energetics of the semidiurnal and diurnal internal tides.

The energy properties of internal tides have recently received attention for their possible role in maintaining ocean mixing. This section describes the energy density and flux of the internal tides observed during AMODE, and compares the energy values to those of the barotropic tide (Wunsch 1975; Schott 1977). The comparison of diurnal baroclinic and barotropic tidal energies highlights the resonant properties of the diurnal waves. The TPXO.5 tidal model of Egbert et al. (1994) is used for the barotropic calculations. Of the many tidal models derived from the TOPEX/Poseidon altimetry data in recent years (Shum et al. 1997), the TPXO model is one of the few that simultaneously solves for elevations and currents in a manner that is consistent with dynamics and uncertainties. For the ocean mixing problem, the baroclinic energies and barotropic dissipation values derived here are quite small compared to more energetic regions of the world's oceans (Egbert and Ray 2000; 2001; 2003).

The ratio of potential to kinetic energy of free, sinusoidal waves is

$$\frac{PE}{KE} = \frac{(\omega^2 - f^2)}{(\omega^2 + f^2)} \quad (7)$$

This ratio is a generic property of internal waves, so long as they can be described by sinusoidal waves and vertical modes. For free waves, the energy flux can be calculated by multiplying the total energy density by the group velocity. For path (2,4) of AMODE, the M_2 amplitude for displacement is about 1.6 m, which corresponds to a potential energy density of 10.3 J m^{-2} . Using (7), a kinetic energy density of 15.2 J m^{-2} is implied. The total energy density is therefore about 25 J m^{-2} , which, using a group velocity of 2.8 ms^{-1} , gives an energy flux of 71 W m^{-1} for northward wavenumbers. The other

semidiurnal constituents, S_2 , N_2 , and K_2 , have negligible energy compared to these values. This energy flux is rather small. Dushaw et al. (1995) found an energy flux of 180 W m^{-1} in the central North Pacific, and energy fluxes near the Hawaiian Ridge of 1000 W m^{-1} or greater have been reported (Ray and Cartwright 2001; Dushaw 2002). Kunze et al. (2003) found 5 kW m^{-1} fluxing upcanyon into Monterey Canyon at the shelf break, and Althaus et al. (2003) find 7 kW m^{-1} radiating away from Mendocino escarpment. Hendry (1977) reported an energy density of 90 J m^{-2} for the M_2 internal tide from the MODE array, based on a root-mean-square amplitude for the 14 moorings of 3.1 m. The thermistor results from AMODE had similar values (Table 5); the superposition of many waves exaggerates the estimated amplitude of the internal waves observed at individual points and leads to an over estimation of energy density and flux.

The diurnal waves are not sinusoidal in the meridional direction, so that the simple ratio (7) cannot be applied to calculate their energy. For these waves, the ratio of potential to kinetic energy is

$$\frac{PE}{KE} = \frac{gD_n \left(\frac{\partial V(y)}{\partial y} \right)^2}{V^2(y)(\omega^2 + f^2)} \quad (8)$$

which can be obtained by applying an integration by parts to the basic equations for internal-wave potential and kinetic energy. This ratio reduces to that for the sinusoidal waves given above, since for such waves $1/gD_n = k_n^2/(\omega^2 - f^2)$ and $\partial V/\partial y = ik_n V$. Standing waves have no energy flux.

Using a displacement amplitude of 1 m for the K_1 internal wave, approximately the measured value, the potential, kinetic, and total energy densities are shown as a function of latitude in Fig. 13 (see also Hendershott 1973). The energy densities for the K_1

barotropic tide are also shown, showing that the internal wave energy density exceeds that of the barotropic tide at many places. Nominal values for the K_1 internal wave at about 25°N are 4.5, 25, and 30 J m^{-2} for potential, kinetic and total energy density, respectively. Nominal values for the K_1 barotropic tide are 12, 3, and 15 J m^{-2} for potential, kinetic and total energy density, respectively. Nominal values for the O_1 constituent internal wave at about 25°N are 1.5, 16, and 18 J m^{-2} for potential, kinetic and total energy density, respectively. Nominal values for the O_1 barotropic tide are 9, 2, and 11 J m^{-2} for potential, kinetic and total energy density, respectively. For both the K_1 and O_1 frequencies, therefore, the ratio of baroclinic to barotropic energy density is 2 to 1. The resonant property of the internal waves is evident; they are generated from the barotropic tide, yet they have greater energy density.

Modern global tidal models can be used to estimate energy flux (e.g. Fig. 14) and the divergence of energy flux. These allow the loss of energy from the barotropic tide in a region to be estimated (Egbert and Ray 2000; 2001; 2003). The energy budget is

$$\text{Net Energy In} = \text{Astronomical Work} + \text{Dissipation} \quad (9)$$

The net energy flux into a particular area can be estimated from the tide models, and the astronomical work is known, so estimation of dissipation is straightforward. The TPXO.5 tidal model was used to estimate the net M_2 energy lost along the Caribbean island chain from Puerto Rico to the Bahamas. The precise estimate of the net dissipation of energy was somewhat uncertain because of the complications of this 3-Mm long island/trench system, but it appears to be 1–2 GW. This value is small compared to other regions of noted tidal dissipation such as Hawaii (Egbert and Ray 2000; 2001; 2003). The 71 W m^{-1} M_2 energy flux estimated to be carried by the internal tide can be used to

estimate the dissipation from the barotropic tide by internal wave radiation. This energy flux is estimated from path (2,4), so it applies to meridional wavenumbers, even though the measurement is obtained within a complicated interference pattern. Other paths measure the energy flux for different wavenumbers, but give similar values for energy flux. While point measurements within the interference pattern would over- or underestimate the energy flux depending on the superposition of wavenumbers, this is not the case for the line-integral measurements. Assuming the 71 W m^{-1} energy flux is a nominal value for wavenumbers of various directions emanating from the whole of the 3-Mm island chain, a net energy loss to the mode-1 internal tide of 0.2 GW is obtained. While this calculation is admittedly crude, it does highlight the relatively small energy loss by internal-tide radiation in this region. The weak radiation may result from the lack of flow over the top of the topography, because the island chain extends to the surface in most places. As discussed by Holloway and Merrifield (1999), Merrifield et al. (2001), and Merrifield and Holloway (2002), internal tide generation is most efficient when the tidal flow is forced across the isobaths of an elongated sub-surface ridge.

Preliminary analyses of internal tides observed by TOPEX/Poseidon near Hawaii have suggested that the mode-1 internal tides have a "decay scale" of 1000 km or longer (Ray and Mitchum 1997). However, much of this "decay" can be accounted for by the change in stratification as the waves move away from the Hawaiian Ridge; the change in stratification gives these waves a weaker surface expression, even if there was no loss of energy by dissipation. Further, the altimeter samples the tides at a meager 10-day interval, so the tidal analysis is likely to be sensitive to any incoherent elements in the internal tides.

The AMODE measurements give a more direct measurement of the decay scale of mode-1 internal tides. There is no evidence for a systematic decrease in tidal amplitude across the tomography array. The parallel paths of the AMODE array are separated by

about 400 km, so that a 1000-km decay scale would suggest that the tidal amplitudes would decrease by a factor of 1.5 over 400-km distance. Assuming the semidiurnal internal tides are propagating and decaying northward away from Puerto Rico, we might expect the amplitude observed on path (1,5) would be reduced, compared to that observed on its parallel path (2,4). In fact, paths (2,4) and (1,5) have M_2 amplitudes of 157 and 194 cm, respectively, so the amplitude appears to have actually increased away from topography. Path (1,5) is shorter than path (2,4), so the larger amplitude observed on path (1,5) may result from its wider beam pattern for semidiurnal radiation. It seems likely that the decay scale of mode-1 internal tides is considerably larger than 1000-km, so that any decay that occurred over the 400-km spacing of the AMODE parallel paths was indistinguishable from the noise in the observations. A very long decay scale is expected theoretically (LeBlond 1966). The long decay scale is also consistent with the existence of the resonant diurnal waves. The resonance requires that the waves propagate from the island chain to the turning latitude and back without appreciable loss of energy. The roundtrip distance is about 2300 km (although this is only 5–6 wavelengths for diurnal constituents).

6. Discussion

Coherent, phase-locked signals of mode-1 semidiurnal (M_2 and N_2) and diurnal (K_1 and O_1) internal tides were observed by a large-scale acoustic tomography array in the western North Atlantic basin. The internal tides had $O(1\text{ m})$ displacements ($O(0.2\text{ cm})$ sea-surface height), hence they were relatively quiescent compared to other regions. Waves traveling in several directions were observed using the antenna properties of the tomographic array. The M_2 and N_2 harmonic constants observed on the various acoustic paths of the tomography array were consistent with the expected properties of the

semidiurnal waves, including wavelengths and "aging". It is difficult to observe these mode-1 waves with thermistors or current meters because of internal wave noise and the difficulties of mode separation. It is apparent that mode-1 internal tides have very weak decay and retain their coherence over great distances, so that ocean basins may be filled up with such waves.

It has sometimes been suggested that temporal variations in buoyancy frequency or currents will cause variations in internal wave properties and so introduce temporal variations in the observed amplitude or phase of internal tides. While the buoyancy suggestion has theoretical appeal, it seems that variations in buoyancy do not significantly affect internal-tide phase stability at least for the lowest mode. Buoyancy variations observed over decades at the Hawaiian Ocean Time series site (Dushaw 2002) had little effect on the low-mode properties (e.g., phase speed) of the internal tides, and the hydrographic data collected during AMODE similarly suggested that low-mode properties were negligibly influenced by changes in stratification. A greater effect from buoyancy variations may occur at the topography features where the internal waves are generated (Mitchum and Chiswell 2000), since buoyancy variations there will directly affect the initial phase of the waves. The doppler effects of ocean currents are also suggested as a reason for the lack of phase stability of internal tides. The magnitude of this effect on low-mode internal tides is unclear, however. Any frequency shifts will occur by *changing* ocean current, and the spatial scales of any variations in current must be comparable to the large scales associated with low-mode internal tides. It seems reasonable to expect a certain stability in the phase or frequency of low-mode internal tides.

A natural question to ask is: If "the internal tide" is so coherent, why is it that the thermistor and altimeter data show a much weaker temporal coherence than the tomography data? A tidal fit to the mode-1 time series derived from the thermistor data accounted for only 7-39% of the variance, while the same fit to the mode-1 time series

derived from tomography accounted for 33-77% of the variance, depending on the strength of the tidal signal in the time series. In the AMODE region, altimetry has detected no internal-tide waves at all. The answer to the question lies in understanding the nature of "the internal tide," together with the properties of the various measurements. "The internal tide" in the AMODE region is obviously composed of a superposition of many different waves propagating in different directions. "The internal tide" is therefore a complicated interference pattern whose stability is likely to be extremely sensitive to any slight variations in the individual waves that make up the pattern. The individual waves can be relatively stable, while the interference pattern can be unstable. The property of a tomographic measurement is that it measures not so much "the internal tide," as the relatively stable wavenumber component perpendicular to the acoustic path. In addition, tomography is a natural measurement of mode-1 only, while the vertical sampling of the thermistor data was so poor that a clear mode-1 time series could not be resolved, i.e., noise in the thermistor data was severe. Altimetry, like the thermistors, is a point-wise measurement of the internal-tide interference pattern, with the added difficulties of relatively weak internal tide signals (when such signals are barely detectable in any region) and of meagre 10-day sampling intervals. When one talks of "the internal tide," it is important to be clear whether one is referring to either the tide composed of a set of wavenumbers, or the tide composed of a single wavenumber.

Recent modeling results for internal tides globally (Simmons et al. 2004; Arbic et al. 2004) highlight the interference patterns of internal tides formed by the interaction of multiple internal tide waves (Fig. 15). This numerical model has a number of simplifications, so it should be considered a qualitative description of the generation and propagation of low-mode internal tides. Nevertheless, the model results of Figure 15 show that the western North Atlantic has internal tides that are relatively weak and consist of the superposition of several waves. Regions of the eastern North Atlantic have relatively

large internal tides, which are known to exist from *in situ* data, but which are not observed by altimetry (Ray and Mitchum 1997; Kantha and Tierney 1997). The interference patterns in the eastern North Atlantic may go undetected by altimetry for the reasons suggested above.

The M_2 internal tide energy density for meridional wavenumbers was 25 J m^{-2} , which corresponds to a northward energy flux of 71 W m^{-1} . The net M_2 energy carried by mode-1 internal waves from the 3-Mm long Caribbean island chain may be about 0.2 GW, with large uncertainty. The M_2 barotropic tide energy dissipation from the island chain (TPXO.5) is 1–2 GW, also with large uncertainty. The western North Atlantic is a weak source of tidal energy available for ocean mixing.

Coherent, resonant diurnal internal tides are trapped between Puerto Rico and 30°N turning latitude. The diurnal amplitudes and phases observed on the various acoustic paths were fit to the meridional structure of these standing internal waves near their turning latitude. The K_1 energy density is $15\text{--}50 \text{ J m}^{-2}$, with an Airy-function type of variation with latitude. The maximum energy density is predicted to occur at about 30°N . The ratio of barotropic tidal amplitudes ($M_2:K_1$) is about 1:0.06, while the observed ratio for internal tide amplitudes is about 1:1. The K_1 energy flux is "0" W m^{-1} , because it is a standing wave. The ratio of barotropic to baroclinic energy is 1 to 2, for both K_1 and O_1 frequencies. Diurnal currents near the critical latitude in the region of AMODE should be greatly enhanced compared to the currents predicted by the global barotropic tide models. Enhanced diurnal currents near the critical latitude were first predicted by Hendershott (1973). Interestingly, the modeling results of Figure 15 suggest a resonant semidiurnal internal tide east of Iceland. The turning latitude for the M_2 frequency is 75°N . Modeling results for the diurnal frequencies are not yet available.

There are many open questions concerning these internal waves. Does their energy dissipate to bottom friction, or does it cascade to higher wavenumbers? What is the

"lifetime" or decay rate of mode-1 internal waves? If 10% of the barotropic tide energy is lost to radiated waves during each diurnal cycle, the 1:2 energy ratio for diurnal waves implies a lifetime of 20 days. What are the details of internal-tide generation, including the effects of the Puerto Rico trench? A future task is to apply a more accurate, regional model for internal tide generation in the western Atlantic to relate the observed tides to their dynamical generation. In particular, an accurate model for diurnal internal tides, when combined with the data reported here, will give a determination of the energy loss, or decay rate, of mode-1 waves in the open ocean. The energy lost from mode-1 waves may be an important driver of deep ocean mixing.

Acknowledgements. The author thanks S. Abbott, K. Bader, T. Birdsall, B. Cornuelle, A. Ganse, K. Hardy, D. Horwitt, B. Howe, R. Knox, S. Leach, B. Ma, G.&E. Marshall, J. Mercer, L. Nielson, R. Odom, B. Paisley, D. Peckham, P. Russo, R. Spindel, R. Truesdale, and P. Worcester who conducted the AMODE experiment with dedication and skill. BDD was supported by NSF grants OCE-9415650 and OCE-9720680. AMODE was funded by ONR contracts N00014-87-K-0760 and N00014-91-J-4055.

APPENDIX A

Normalization of Internal Wave Modes

The derivation of internal wave modes and internal wave properties is described many places (e.g., LeBlond and Mysak 1978; Hendershott 1981). The relevant equations were reviewed in Dushaw et al. (1995); here the normalization and nominal mode amplitudes particular to this paper are given. The equation for the displacement modes of low-frequency internal waves is

$$\frac{d^2 F_n(z)}{dz^2} + \lambda_n N^2(z) F_n(z) = 0 \quad (\text{A1})$$

with boundary conditions

$$\frac{dF_n(z)}{dz} - g \lambda_n F_n(z) = 0 \quad \text{at } z = 0 \quad (\text{A2})$$

$$F_n(z) = 0 \quad \text{at } z = D \quad (\text{A3})$$

Because the tidal frequencies are low for internal waves, this equation is the low-frequency limit of the equation for internal wave modes; it is frequency independent. The eigenvalues, λ_n , are sometimes written as $1/(g D_n)$, where D_n is the "equivalent depth" of the mode.

The normalization of the displacement modes $F_n(z)$ is

$$\int_D^0 F_n^2(z) N^2(z) dz = D \bar{N}^2 \quad (\text{A4})$$

where

$$\bar{N} = \frac{1}{D} \int_D^0 N(z) dz \quad (\text{A5})$$

and D is ocean depth. With this normalization, the mode-1 displacement mode with 1-m amplitude had a surface value of -1.6×10^{-3} m and a maximum value at mode-maxium at 1300-m depth of +1.15 m. Tables 4 and 5 use units of centimeters for convenience; in those tables "100 cm" amplitude corresponds to a vertical displacement of 1.15 m. The modes in temperature or sound speed are obtained by multiplying the displacement modes by the negative of potential temperature or sound speed gradient. Hydrographic data obtained during AMODE were used to derive the buoyancy and potential temperature and sound speed gradients for these calculations.

REFERENCES

- Abramowitz, M., and Stegun I. A. (Eds.), 1965. *Handbook of Mathematical Functions*, National Bureau of Standards, Washington, D.C..
- The Acoustic Mid-Ocean Dynamics Experiment Group, 1994. Moving ship tomography in the northwest Atlantic Ocean. *Eos, Transactions of the American Geophysical Union*, **75**, 17, 21, 23.
- Althaus, A. M., Kunze, E., and Sanford, T. B., 2003. Internal tide radiation from Mendocino Escarpment, *Journal of Physical Oceanography*, **33**, 1510–1527.
- Arbic, B., Garner, S., Hallberg, R., Simmons, H., 2004. The accuracy of surface elevation in forward global barotropic and baroclinic tide models. *Deep-Sea Research II*, **51**, 3069–3101.
- Bracher, C., and Flatté, S., 1997. A baroclinic tide in the eastern North Pacific determined from 1000-km acoustic transmissions. *Journal of Physical Oceanography*, **27**, 485–497.
- Cornuelle, B. D. and Worcester, P. F., 1996. Ocean acoustic tomography: Integral data and ocean models. In: *Modern Approaches to Data Assimilation in Ocean Modeling*, P. Malanotte-Rizzoli, ed., Elsevier Science, pp. 97–115.
- Clark, J. G., and Kronengold, M., 1974. Long-period fluctuations of CW signals in deep and shallow water. *Journal of the Acoustical Society of America*, **56**, 1071–1083.

- Cummins, P. F., Cherniawsky, J. Y., and Foreman, M. G. G., 2001. North Pacific internal tides from the Aleutian Ridge: Altimeter observations and modeling. *Journal of Marine Research*, **59**, 167–191.
- Dushaw, B. D., 2002. Mapping low-mode internal tides near Hawaii using TOPEX/POSEIDON altimeter data. *Geophysical Research Letters*, **29**, 10.1029/2001GL013944.
- Dushaw, B. D., 2003. On the mapping and wavenumber resolution of line-integral data for observations of low-mode internal tides. *Journal of Oceanic and Atmospheric Technology*, **20**, 1043–1059.
- Dushaw, B. D., and Worcester, P. F., 1998. Resonant diurnal internal tides in the North Atlantic. *Geophysical Research Letters*, **25**, 2189–2192.
- Dushaw, B. D., Cornuelle, B. D., Worcester, P. F., Howe, B. M., and Luther, D. S., 1995. Barotropic and baroclinic tides in the central North Pacific Ocean determined from long-range reciprocal acoustic transmissions. *Journal of Physical Oceanography*, **25**, 631–647.
- Dushaw, B. D., Worcester, P. F., Cornuelle, B. D., Marshall, A. R., Howe, B. M., Leach, S., Mercer, J. A., and Spindel, R. C., 1996. Data report: Acoustic Mid-Ocean Dynamics Experiment (AMODE). APL-UW TM 2-96. Applied Physics Laboratory, University of Washington, Seattle, Washington, 275 pp.
- Dushaw, B. D., Egbert, G. D., Worcester, P. F., Cornuelle, B. D., Howe, B. M., and

- Metzger, K., 1997. A TOPEX/POSEIDON global tidal model (TPXO.2) and barotropic tidal currents determined from long-range acoustic transmissions. *Progress in Oceanography*, **40**, 337–367.
- Dyson, F., Munk, W., and Zetler, B., 1976. Interpretation of multipath scintillations to Eleuthera to Bermuda in terms of internal waves and tides. *Journal of the Acoustical Society of America*, **59**, 1121–1133.
- Egbert, G. D., and Ray, R. D., 2000. Significant dissipation of tidal energy in the deep ocean inferred from satellite altimeter data, *Nature*, **405**, 775–778.
- Egbert, G. D., and Ray, R. D., 2001. Estimates of M2 tidal energy dissipation from Topex/Poseidon altimeter data, *Journal of Geophysical Research*, **106**, 22 475–22 502.
- Egbert, G. D. and Ray, R. D., 2003. Semi-diurnal and diurnal tidal dissipation from Topex/Poseidon altimetry, *Geophysical Research Letters*, **30(17)**, 1907.
- Egbert, G. D., Bennett, A. F., and Foreman, M. G. G., 1994. TOPEX/POSEIDON tides estimated using a global inverse model. *Journal of Geophysical Research*, **99**, 24 821–24 852.
- Hendershott, M. C., 1973. Inertial oscillations of tidal period. *Progress in Oceanography*, vol. 6, 1–27.
- Hendershott, M. C., 1981. Long waves and ocean tides. In *Evolution of Physical Oceanography*, B. A. Warren and C. Wunsch, Eds., The MIT Press, 292–341.

- Hendry, R. M., 1977. Observations of the semidiurnal internal tide in the western North Atlantic ocean. *Philosophical Transactions of the Royal Society*, **A286**, 1–24.
- Holloway, P.E. and Merrifield, M., 1999. Internal tide generation by seamounts ridges and islands. *Journal of Geophysical Research*, **104**, 25937–25951.
- Jobst, W., and Dominijanni, L. 1979. Measurements of the temporal, spatial, and frequency stability of an underwater acoustic channel. *Journal of the Acoustical Society of America*, **65**, 62–69.
- Kang, S. K., Foreman, M. G. G., Crawford, W. R., and Cherniawsky, J. Y., 2000. Numerical modeling of internal tide generation along the Hawaiian Ridge. *Journal of Physical Oceanography*, **30**, 1083–1098.
- Kantha, L. H., and Tierney, C. C., 1997. Global baroclinic tides. *Progress in Oceanography*, **40**, 163–178.
- Kunze, E., Rosenfeld, L. K., Carter, G. S., Gregg, M. C., 2002. Internal waves in Monterey submarine canyon. *Journal of Physical Oceanography*, **32**, 1890–1913.
- LeBlond, P. H., 1966. On the damping of internal gravity waves in a continuously stratified ocean. *Journal of Fluid Mechanics*, **25**, 121–142.
- LeBlond, P. H., and Mysak, L. A., 1978. *Waves in the Ocean*. Elsevier, 602 pp.
- Merrifield, M. A., and Holloway, P. E., 2002. Model estimates of M_2 internal tide

- energetics at the Hawaiian Ridge. *Journal of Geophysical Research*, **107**, 10.1029/2001JC000996.
- Merrifield, M. A., Holloway, P. E., and Shaun Johnston, T. M., 2001. The generation of internal tides at the Hawaiian Ridge. *Geophysical Research Letters*, **28**, 559–562.
- Mitchum, G. T., and Chiswell, S., 2000. Coherence of internal tide variations along the Hawaiian Ridge. *Journal of Geophysical Research*, **105**, 28 653–28 661, 2000.
- Munk, W., and Wunsch, C., 1998. Abyssal Recipes II: energetics of tidal and wind mixing, *Deep-Sea Research I*, **45**, 1976–2000.
- Munk, W., Worcester, P., and Wunsch, C., 1995. *Ocean Acoustic Tomography*, Cambridge University Press, Cambridge.
- Munk, W., Zetler, B., Clark, J., Gill, S., Porter, D., Spiesberger, J., and Spindel, R., 1981. Tidal effects on long-range sound transmission. *Journal of Geophysical Research*, **86**, 6399–6410.
- Philander, S. G. H., 1977. The effects of coastal geometry on equatorial waves (Forced waves in the Gulf of Guinea). *Journal of Marine Research*, **35**, 509–523.
- Philander, S. G. H., 1978. Forced oceanic waves. *Reviews of Geophysics and Space Physics*, **16**, 15–46.
- Pinkel, R., Munk, W., Worcester, P., Cornuelle, B. D., Rudnick, D., Sherman, J., Filloux,

- J. H., Dushaw, B. D., Howe, B. M., Sanford, T. B., Lee, C. M., Kunze, E., Gregg, M. C., Miller, J. B., Moum, J. M., Caldwell, D. R., Levine, M. D., Boyd, T., Egbert, G. D., Merrifield, M. A., Luther, D. S., Firing, E., Brainard, R., Flament, P. J., and Chave, A. D., 2000. Ocean mixing studied near Hawaiian Ridge. *EOS, Transactions of the American Geophysical Union*, **81**, pp. 545,553.
- Ray, R. D., and Cartwright, D. E., 2001. Estimates of internal tide energy fluxes from Topex/Poseidon altimetry: Central North Pacific. *Geophysical Research Letters*, **28**, 1259–1262.
- Ray, R. D., and Mitchum, G. T., 1996. Surface manifestation of internal tides generated near Hawaii. *Geophysical Research Letters*, **23**, 2101–2104.
- Ray, R. D., and Mitchum, G. T., 1997. Surface manifestation of internal tides in the deep ocean: Observations from altimetry and island gauges. *Progress in Oceanography*, **40**, 337–367.
- Schott, F., 1977. On the energetics of baroclinic tides in the North Atlantic. *Annales Géophysique*, **33**, 41–62.
- Schureman, P., 1958. Manual of harmonic analysis and prediction of tides. Spec. Publ. 98, U.S. Govt. Printing Office, 317 pp.
- Shum, C. K., Woodworth, P. L., Anderson, O. B., Egbert, G., Francis, O., King, C., Klosko, S., LeProvost, C., Li, X., Molines, J., Parke, M., Ray, R., Schlax, M., Stammer, D., Tierney, C., Vincent, P., and Wunsch, C., 1997. Accuracy assessment of recent

ocean tide models. *Journal of Geophysical Research*, **102**, 25 173–25194.

Simmons, H. L., Hallberg, R. W., and Arbic B. K., 2004. Internal wave generation in a global baroclinic tide model. *Deep-Sea Research II*, **51**, 3043–3068.

Sjoberg, B., and Stigebrandt, A., 1992. Computations of the geographical distribution of the energy flux to mixing processes via internal tides and the associated vertical circulation in the ocean. *Deep-Sea Research*, **39**, 269–291.

Weinberg, N. L., Clark, J., and Flanagan, R. P., 1974. Internal tidal influence on deep-ocean acoustic-ray propagation. *Journal of the Acoustical Society of America*, **56**, 895–905.

Wunsch, C., 1975. Internal tides in the ocean. *Reviews of Geophysics and Space Physics*, **13**, 167–182.

Wunsch, C., and Gill, A. E., 1976. Observations of equatorially trapped waves in Pacific sea level variations. *Deep-Sea Research*, **23**, 371–390.

CAPTIONS

FIG. 1. The AMODE array was located midway between Puerto Rico and Bermuda. The heavy lines show contours of bottom topography at 1000 m intervals. The dotted and dashed lines show the amplitude (in cm) and phase (in degrees), respectively, of the M_2 barotropic tidal elevation from the tidal model of Egbert et al. (1994) (TPXO.5 version). The phase of the tide is fairly constant along the continental shelf and Caribbean island arc. The concentric circles to the northwest of the tomography array show the location of the 16 moorings of the MODE experiment (Hendry 1977).

FIG. 2. A meridional section of topography through the AMODE array showing the locations of Puerto Rico, the Puerto Rico Trench, and Bermuda. The set of ray paths from the acoustic path between moorings 1 and 3 are shown. (left) Corresponding sound speed profile, and (right) the first three temperature modes of internal waves. The three dots in the panel at right show the approximate locations of the three thermistors on each mooring.

FIG. 3. High-frequency (> 1 cpd) travel time data obtained on the acoustic paths indicated in the upper right of each panel. The sum of reciprocal-ray travel times, a measure of sound speed variability, are shown. 8–12 rays are resolved on each acoustic path; the several time series in each panel show the travel times associated with the resolved ray paths. The tidal variability of the travel times in each panel is nearly identical because the signals are dominated by mode-1 internal tides. Note that some paths (e.g., 2,4) are dominated by semidiurnal variability, while other paths (e.g., 2,3) are dominated by diurnal variability. These 40-day sections of the time series show the more frequent transmissions during the Moving Ship Tomography experiment followed by the regular transmissions on every fourth day.

FIG. 4. Spectra of the time series of mode-1 amplitude derived from the thermistor data obtained on moorings 1 and 3 as indicated. Tidal lines are obvious in these spectra, but there is no apparent geographical pattern to the intensity of the lines. As discussed in the text, the intensities of the lines for the diurnal frequencies appear to be comparable to those of the semidiurnal frequencies.

FIG. 5. (a) Part of the time series of mode-1 amplitude derived from the travel times obtained on path (2,4) (heavy line). The tidal fit to the data is also shown (light line). Only 45 days of the 181-day record length are shown. (b) The residual of the time series after removing the tides. The tidal fit accounts for 77% of the variance. Residual tidal variability is evident, perhaps caused by incoherent components of the internal tide.

FIG. 6. The difference between the M_2 and N_2 internal tide phases obtained on the 15 acoustic paths. The dotted line shows the phase difference between the M_2 and N_2 barotropic tides. The internal tide phase differences are consistent with propagation of a few hundred kilometers, although the uncertainties are so large as to preclude definitive conclusions.

FIG. 7. Maps of the mode-1 amplitude of the M_2 internal tide observed by the AMODE array. The cosine component of the field (top left) propagates from the northwest to the southeast, while the sine component of the field (top right) propagates meridionally (see also Dushaw (2003)). This solution for the tidal field assumes that the internal tide is propagating away from the nearest topography. The *a priori* wavenumber spectrum (bottom left) is chosen to give wavenumbers away from topography in the solution. The spectrum estimated from the objective map is also shown (bottom right). [Modified from Dushaw (2003).]

FIG. 8. The K_1 barotropic tidal elevation from the tidal model of Egbert et al. (1994) (TPXO.5 version). The dotted and dashed lines show the amplitude (in cm) and phase (in degrees), respectively. The phase of the diurnal tide changes by only about 20°

along the Caribbean island arc.

FIG. 9. Eigenfrequencies of (6) as a function of mode number determined by "shooting". The K_1 and O_1 frequencies are consistent with the eigenfrequencies, but the match is not exact.

FIG. 10. Current and displacement modes as a function of latitude for the K_1 and O_1 constituents determined from the equatorial beta plane solutions (dashed; orders 42 and 36) and numerical solutions (solid; orders 5 and 3). The approximate and numerical solutions are similar and probably cannot be distinguished by the acoustic data. The locations of the 6 AMODE moorings are indicated in the panels for the displacement modes. A wave for semidiurnal frequencies (150-km wavelength) is shown in the top panel.

FIG. 11. The panels at left show the predicted displacement of diurnal waves at the K_1 and O_1 frequencies, together with the measured harmonic constants for each acoustic path. The panels at right show the predicted displacement as a function of latitude, together with the harmonic constants determined from the thermistor data obtained on each mooring. The horizontal dotted line in the panel for O_1 indicates the turning latitude. The boundary condition at 19–20 °N is zero meridional flow; which corresponds to maximum displacement. [From Dushaw and Worcester 1998.]

FIG. 12. Comparison of predicted resonant wave harmonic constants of the internal tide to measured harmonic constants (with error bars) for the (top) K_1 and (bottom) O_1 frequencies. For each comparison only two parameters (an amplitude and a phase) of the predicted wave are adjusted to fit to the 30 independent data. The harmonic constants are plotted as a function of the azimuthal angle of orientation of their acoustic path; zonal paths are at 0°.

FIG. 13. Potential (top), kinetic (middle), and total energy of the K_1 internal tide as a function of latitude. The kinetic energy is inferred from the displacement. The barotropic energy is shown by the horizontal dashed line, showing that in some latitude

bands the internal tide energy is many times larger than the barotropic energy for this frequency.

FIG. 14. M_2 barotropic tidal energy flux derived from the tidal model of Egbert et al. (1994) (TPXO.5 version). The tides are fairly large over the continental shelf of the United States; the lack of energy flux shows that the tide there is a standing wave.

FIG. 15. The state of M_2 baroclinic tide radiation 20 days after the start of the Simmons et al. (2004) model run in the North Atlantic. According to this model, the M_2 internal tides are relatively weak in the AMODE region compared to other areas. Resonant M_2 internal tides are possibly evident east of Iceland, presumably trapped between topography and their 75°N turning latitude. Modified from Simmons et al. (2004).

Table 1. The AMODE transceiver mooring positions and their uncertainties.

Mooring	Latitude (North)	Uncert. (m)	Longitude (West)	Uncert. (m)	Source Depth (m)
1	27°43.2329'	0.6	64°31.1107'	0.9	985
2	24°20.0499'	0.5	62°53.3477'	0.8	996
3	21°53.9489'	0.5	65°49.8894'	0.8	1003
4	23°38.2722'	0.5	69°21.5593'	0.8	1008
5	27°21.1214'	0.6	68°43.5229'	0.9	979
6	25°00.0178'	0.5	66°15.0826'	0.8	992

Table 2. Values for the harmonic constants (amplitude and phase) of the barotropic tide elevation and currents. These values were derived from the TPXO.5 tidal model for the position of the central AMODE mooring.

Constituent	Elevation (cm)	Zonal Current (cm/s)	Meridional Current (cm/s)
K_2	1.4 28°	0.07 123°	0.06 327°
S_2	4.6 25°	0.22 122°	0.21 328°
M_2	25.7 2°	1.09 100°	0.82 292°
N_2	5.8 341°	0.25 80°	0.19 271°
K_1	7.0 200°	0.08 279°	0.15 55°
P_1	2.2 200°	0.01 300°	0.04 64°
O_1	5.7 205°	0.01 301°	0.08 61°
Q_1	1.1 193°	0.00 83°	0.02 58°

Table 3. Internal-tide phase speed (s), group speed (s_g), wavelength (λ), and wavenumber (k) at 25°N derived from hydrographic data obtained in the AMODE region.

Mode	Constituent	s (m/s)	s_g	λ (km)	k ($\times 10^{-2}$ rad/km)
1	M ₂	3.34	2.70	150	4.20
	S ₂	3.32	2.73	143	4.38
	N ₂	3.36	2.69	153	4.10
	K ₁	5.59	1.62	482	1.30
	O ₁	7.22	1.25	672	0.94
2	M ₂	1.46	1.18	65	9.60
	S ₂	1.45	1.19	63	10.02
	N ₂	1.47	1.18	67	9.38
	K ₁	2.45	0.71	211	2.98
	O ₁	3.16	0.55	294	2.14
3	M ₂	1.08	0.88	48	12.97
	S ₂	1.08	0.88	46	13.53
	N ₂	1.09	0.87	50	12.67
	K ₁	1.81	0.52	156	4.03
	O ₁	2.34	0.41	218	2.89

Table 4. Amplitudes and Greenwich phases of the mode-1 baroclinic tide measured on each of the 15 acoustic paths of the AMODE array. Values are given for the frequencies of the eight major tidal constituents. The acoustic path is denoted by the pair of numbers, e.g., "(1,2)" is the path between moorings 1 and 2. The locations of the mooring are given in Figure 1 and Table 1. The percent of the time series variance accounted for by the tidal fit is also given. The normalization of mode 1 is such that an amplitude of 1 m roughly corresponds to a vertical displacement of 1 m at mode maximum (see Appendix A). The uncertainties of the amplitudes are 4–8 cm.

Acoustic Path	Record Length (d)	% Tidal	Amplitude (cm)							
			K_2	S_2	M_2	N_2	K_1	P_1	O_1	Q_1
1,2	181	70%	23	18	123	21	44	16	25	15
1,3	189	69%	8	16	72	31	69	25	17	5
1,4	189	34%	7	8	37	12	30	5	26	10
1,5	101	69%	10	14	194	34	49	15	17	16
1,6	188	59%	12	22	125	9	85	21	26	10
2,3	333	33%	20	12	48	4	36	20	32	24
2,4	181	77%	6	30	157	45	94	21	64	19
2,5	250	32%	5	30	67	32	51	16	16	13
2,6	332	45%	3	16	89	28	101	27	53	12
3,4	217	53%	15	18	110	25	53	8	17	34
3,5	178	43%	11	9	49	11	9	5	33	4
3,6	357	38%	13	22	62	30	46	14	23	12
4,5	137	57%	6	35	104	41	53	44	23	12
4,6	213	42%	10	6	9	17	76	23	75	23
5,6	258	33%	28	15	86	12	76	28	34	4

Acoustic Path	Greenwich Phase ($^{\circ}$)							
	K_2	S_2	M_2	N_2	K_1	P_1	O_1	Q_1
1,2	43 \pm 11	316 \pm 14	115 \pm 2	62 \pm 11	86 \pm 6	82 \pm 15	250 \pm 10	201 \pm 15
1,3	79 \pm 25	148 \pm 14	335 \pm 3	271 \pm 7	71 \pm 3	52 \pm 9	215 \pm 12	109 \pm 40
1,4	144 \pm 29	127 \pm 25	309 \pm 6	301 \pm 18	26 \pm 8	10 \pm 37	137 \pm 8	72 \pm 20
1,5	293 \pm 46	21 \pm 35	112 \pm 2	102 \pm 13	89 \pm 11	66 \pm 34	276 \pm 25	185 \pm 27
1,6	27 \pm 26	303 \pm 16	137 \pm 3	3 \pm 34	46 \pm 4	28 \pm 16	198 \pm 12	121 \pm 29
2,3	299 \pm 14	25 \pm 24	109 \pm 6	62 \pm 58	148 \pm 8	99 \pm 15	35 \pm 9	350 \pm 12
2,4	3 \pm 47	56 \pm 11	284 \pm 2	245 \pm 7	252 \pm 3	200 \pm 15	154 \pm 5	358 \pm 16
2,5	294 \pm 59	234 \pm 13	69 \pm 6	2 \pm 12	314 \pm 8	277 \pm 23	214 \pm 23	211 \pm 27
2,6	241 \pm 91	8 \pm 22	267 \pm 4	217 \pm 12	263 \pm 4	282 \pm 13	153 \pm 7	239 \pm 27
3,4	291 \pm 22	327 \pm 19	239 \pm 3	170 \pm 13	110 \pm 6	115 \pm 40	349 \pm 19	19 \pm 10
3,5	212 \pm 23	169 \pm 29	295 \pm 5	253 \pm 21	20 \pm 26	13 \pm 47	118 \pm 7	69 \pm 46
3,6	307 \pm 19	9 \pm 13	202 \pm 4	170 \pm 9	53 \pm 6	25 \pm 18	168 \pm 11	87 \pm 20
4,5	63 \pm 53	338 \pm 11	148 \pm 4	104 \pm 9	70 \pm 7	138 \pm 9	4 \pm 16	349 \pm 29
4,6	172 \pm 31	325 \pm 45	76 \pm 35	105 \pm 20	282 \pm 5	241 \pm 14	145 \pm 5	48 \pm 15
5,6	330 \pm 16	241 \pm 28	79 \pm 5	39 \pm 33	326 \pm 6	206 \pm 16	164 \pm 13	225 \pm 84

Table 5. Amplitudes and Greenwich phases of the mode-1 baroclinic tide measured by thermistors on each of the 6 moorings of the AMODE array, as for Table 4. The uncertainties of the amplitudes are 5–7 cm.

Mooring Number	Record Length (d)	% Tidal	Amplitude (cm)							
			K_2	S_2	M_2	N_2	K_1	P_1	O_1	Q_1
1	339	9%	26	36	121	28	49	53	40	10
2	310	11%	37	59	32	72	91	50	36	12
3	357	29%	8	24	297	67	122	62	126	42
4	310	7%	26	78	108	54	37	30	27	29
5	357	32%	38	83	332	92	85	46	27	27
6	356	39%	31	65	346	68	86	30	103	20

Mooring Number	Greenwich Phase ($^\circ$)							
	K_2	S_2	M_2	N_2	K_1	P_1	O_1	Q_1
1	139 ± 12	16 ± 9	126 ± 3	84 ± 11	92 ± 7	101 ± 6	319 ± 8	83 ± 30
2	38 ± 8	353 ± 5	190 ± 9	236 ± 4	277 ± 3	225 ± 6	118 ± 8	302 ± 22
3	199 ± 41	98 ± 14	219 ± 1	193 ± 5	48 ± 3	57 ± 6	326 ± 3	258 ± 8
4	203 ± 15	16 ± 5	187 ± 4	306 ± 7	51 ± 10	59 ± 13	340 ± 14	11 ± 13
5	240 ± 9	214 ± 4	87 ± 1	30 ± 4	138 ± 4	70 ± 7	54 ± 12	311 ± 12
6	319 ± 9	313 ± 5	189 ± 1	144 ± 4	327 ± 3	251 ± 10	159 ± 3	108 ± 15

Table 6. Amplitudes and Greenwich phases of the M_2 mode-1 baroclinic tide measured for each pair of parallel acoustic paths of the AMODE array.

Path	% Tidal	Amplitude (cm)	Phase ($^{\circ}$ G)	Phase Difference
1,5	69%	194	112 \pm 2	
2,4	77%	157	284 \pm 2	172 \pm 3 $^{\circ}$
1,2	70%	123	115 \pm 2	
3,5	43%	49	295 \pm 5	180 \pm 5 $^{\circ}$
2,3	33%	48	109 \pm 6	
1,4	34%	37	309 \pm 6	200 \pm 8 $^{\circ}$
3,4	53%	110	239 \pm 3	
2,5	32%	67	69 \pm 6	190 \pm 7 $^{\circ}$
4,5	57%	104	148 \pm 4	
1,3	69%	72	335 \pm 3	187 \pm 5 $^{\circ}$

Table 7. Amplitudes and Greenwich phases of the N_2 mode-1 baroclinic tide measured for each pair of parallel acoustic paths of the AMODE array.

Path	% Tidal	Amplitude (cm)	Phase ($^{\circ}$ G)	Phase Difference
1,5	69%	34	102 \pm 13	
2,4	77%	45	245 \pm 7	217 \pm 15 $^{\circ}$
1,2	70%	21	62 \pm 11	
3,5	43%	11	253 \pm 21	169 \pm 24 $^{\circ}$
2,3	33%	4	62 \pm 58	
1,4	34%	12	301 \pm 18	121 \pm 61 $^{\circ}$
3,4	53%	25	170 \pm 13	
2,5	32%	32	2 \pm 12	169 \pm 18 $^{\circ}$
4,5	57%	41	104 \pm 9	
1,3	69%	31	271 \pm 7	193 \pm 11 $^{\circ}$

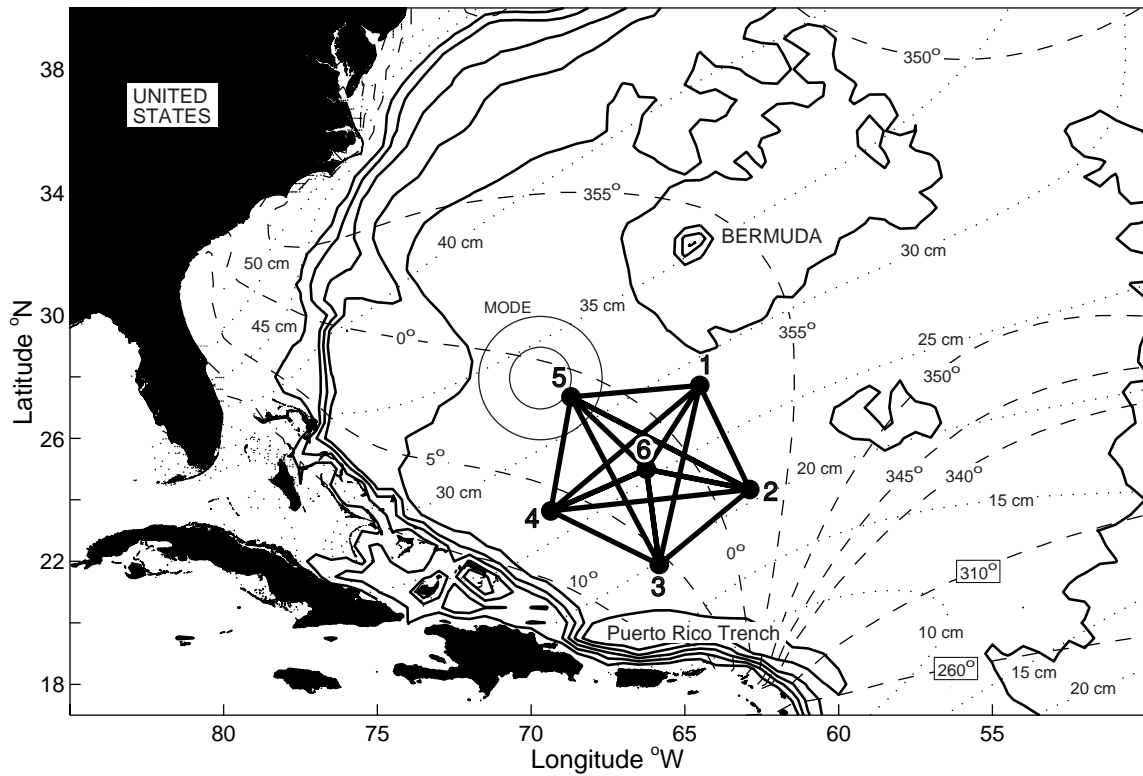


FIG. 1. The AMODE array was located midway between Puerto Rico and Bermuda. The heavy lines show contours of bottom topography at 1000 m intervals. The dotted and dashed lines show the amplitude (in cm) and phase (in degrees), respectively, of the M_2 barotropic tidal elevation from the tidal model of Egbert et al. (1994) (TPXO.5 version). The phase of the tide is fairly constant along the continental shelf and Caribbean island arc. The concentric circles to the northwest of the tomography array show the location of the 16 moorings of the MODE experiment (Hendry 1977).

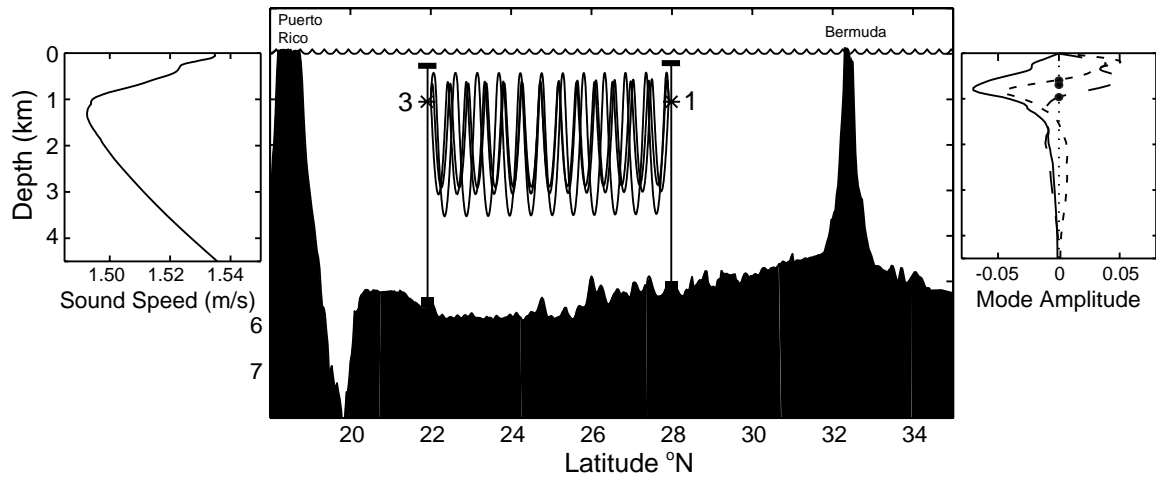


FIG. 2. A meridional section of topography through the AMODE array showing the locations of Puerto Rico, the Puerto Rico Trench, and Bermuda. The set of ray paths from the acoustic path between moorings 1 and 3 are shown. (left) Corresponding sound speed profile, and (right) the first three temperature modes of internal waves. The three dots in the panel at right show the approximate locations of the three thermistors on each mooring.

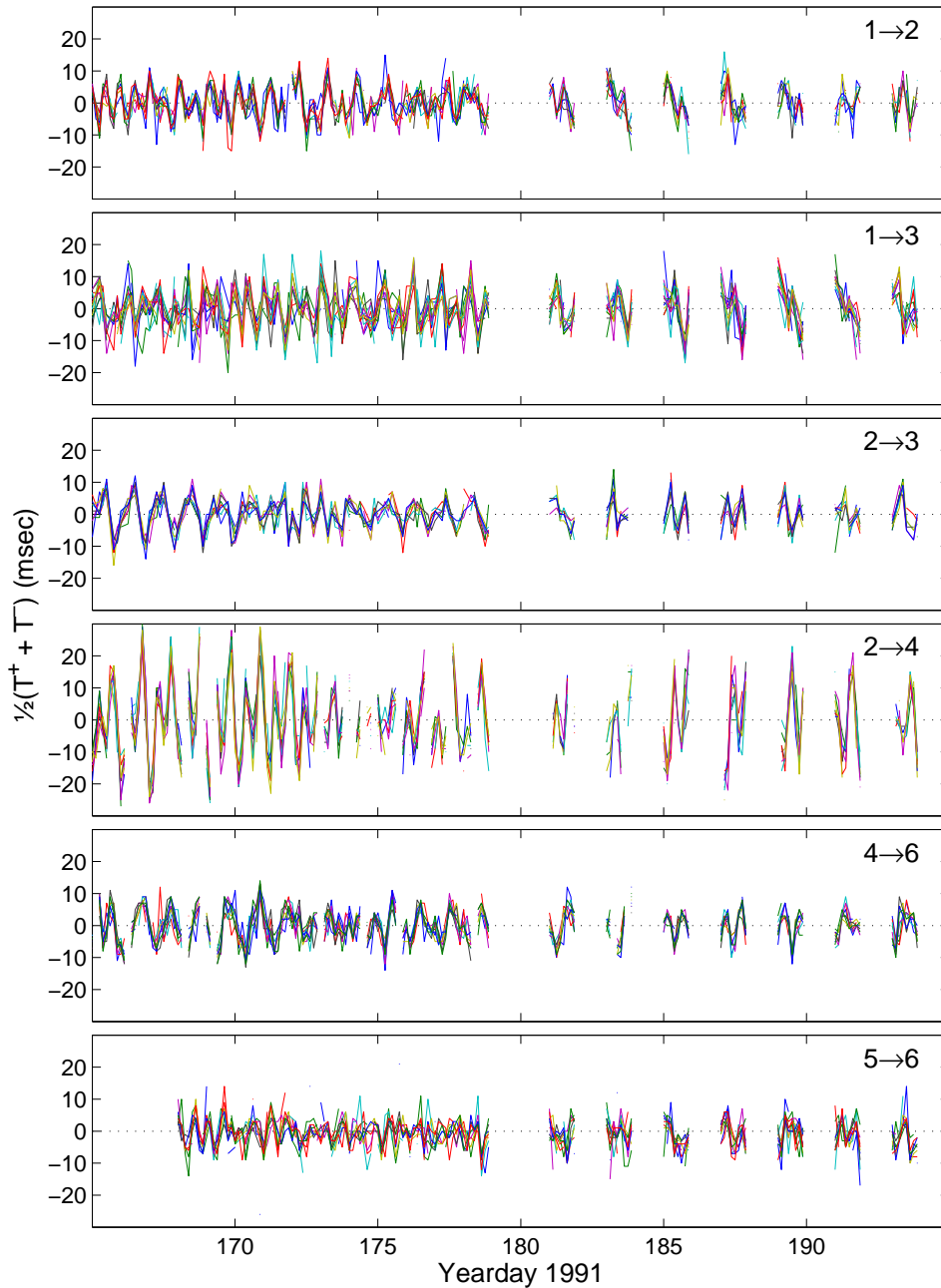


FIG. 3. High-frequency (> 1 cpd) travel time data obtained on the acoustic paths indicated in the upper right of each panel. The sum of reciprocal-ray travel times, a measure of sound speed variability, are shown. 8–12 rays are resolved on each acoustic path; the several time series in each panel show the travel times associated with the resolved ray paths. The tidal variability of the travel times in each panel is nearly identical because the signals are dominated by mode-1 internal tides. Note that some paths (e.g., 2,4) are dominated by semidiurnal variability, while other paths (e.g., 2,3) are dominated by diurnal variability. These 40-day sections of the time series show the more frequent transmissions during the Moving Ship Tomography experiment followed by the regular transmissions on every fourth day.

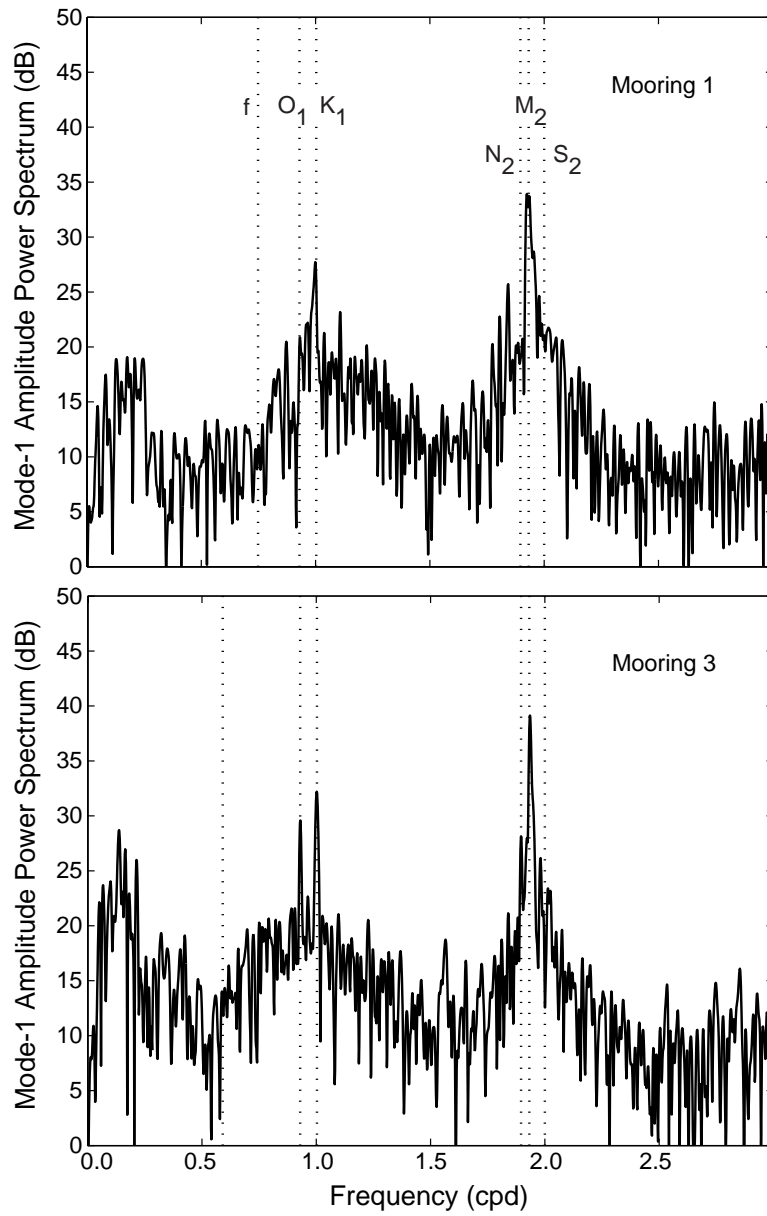


FIG. 4. Spectra of the time series of mode-1 amplitude derived from the thermistor data obtained on moorings 1 and 3 as indicated. Tidal lines are obvious in these spectra, but there is no apparent geographical pattern to the intensity of the lines. As discussed in the text, the intensities of the lines for the diurnal frequencies appear to be comparable to those of the semidiurnal frequencies.

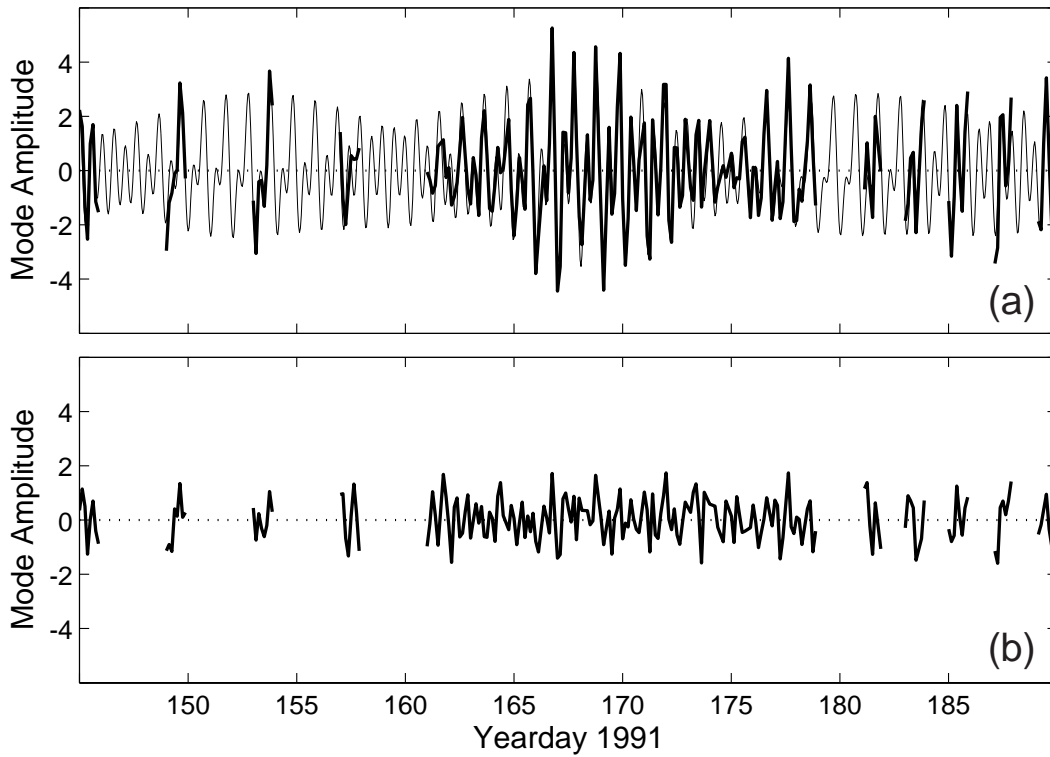


FIG. 5. (a) Part of the time series of mode-1 amplitude derived from the travel times obtained on path (2,4) (heavy line). The tidal fit to the data is also shown (light line). Only 45 days of the 181-day record length are shown. (b) The residual of the time series after removing the tides. The tidal fit accounts for 77% of the variance. Residual tidal variability is evident, perhaps caused by incoherent components of the internal tide.

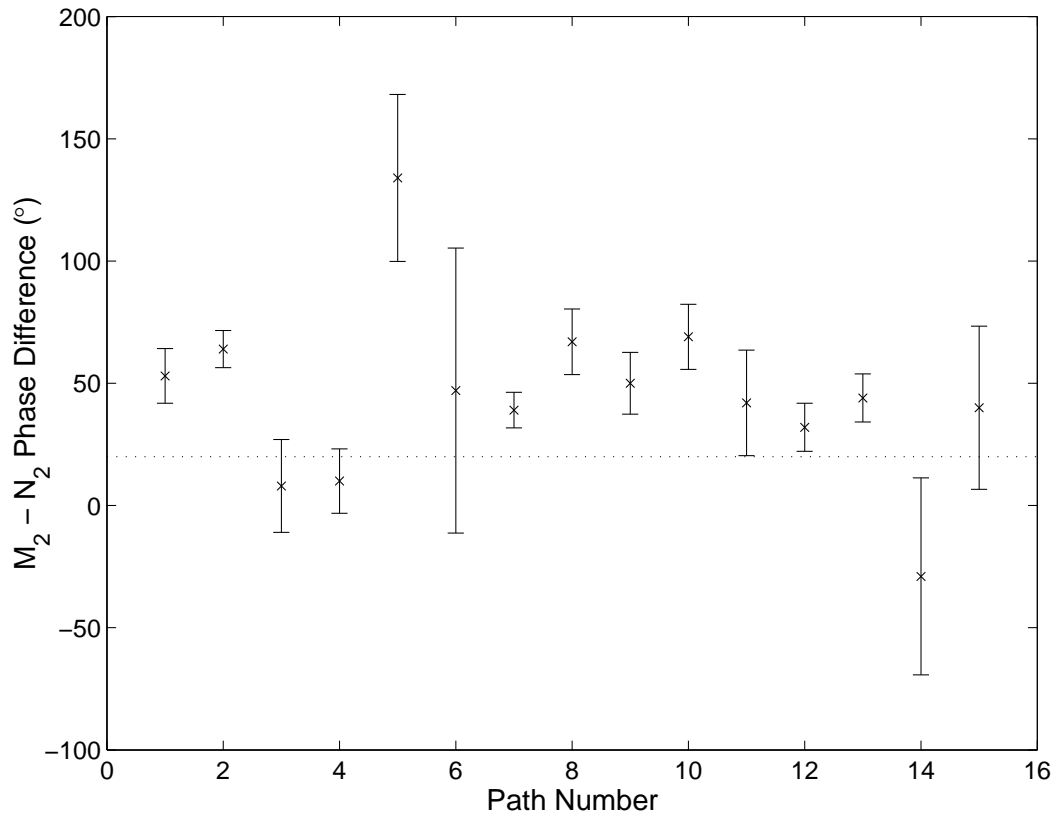


FIG. 6. The difference between the M_2 and N_2 internal tide phases obtained on the 15 acoustic paths. The dotted line shows the phase difference between the M_2 and N_2 barotropic tides. The internal tide phase differences are consistent with propagation of a few hundred kilometers, although the uncertainties are so large as to preclude definitive conclusions.

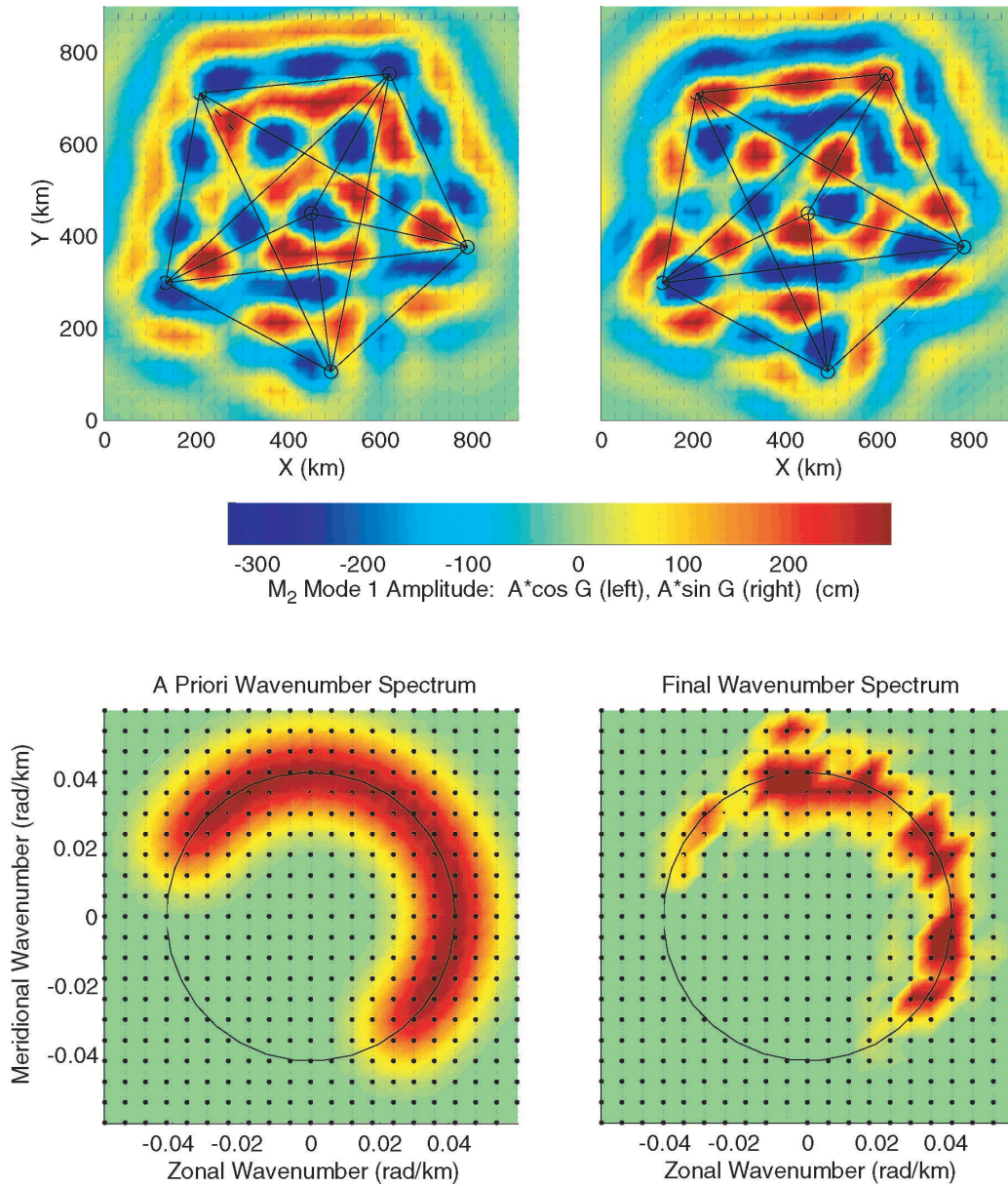


FIG. 7. Maps of the mode-1 amplitude of the M_2 internal tide observed by the AMODE array. The cosine component of the field (top left) propagates from the northwest to the southeast, while the sine component of the field (top right) propagates meridionally (see also Dushaw (2003)). This solution for the tidal field assumes that the internal tide is propagating away from the nearest topography. The *a priori* wavenumber spectrum (bottom left) is chosen to give wavenumbers away from topography in the solution. The spectrum estimated from the objective map is also shown (bottom right). [Modified from Dushaw (2003).]

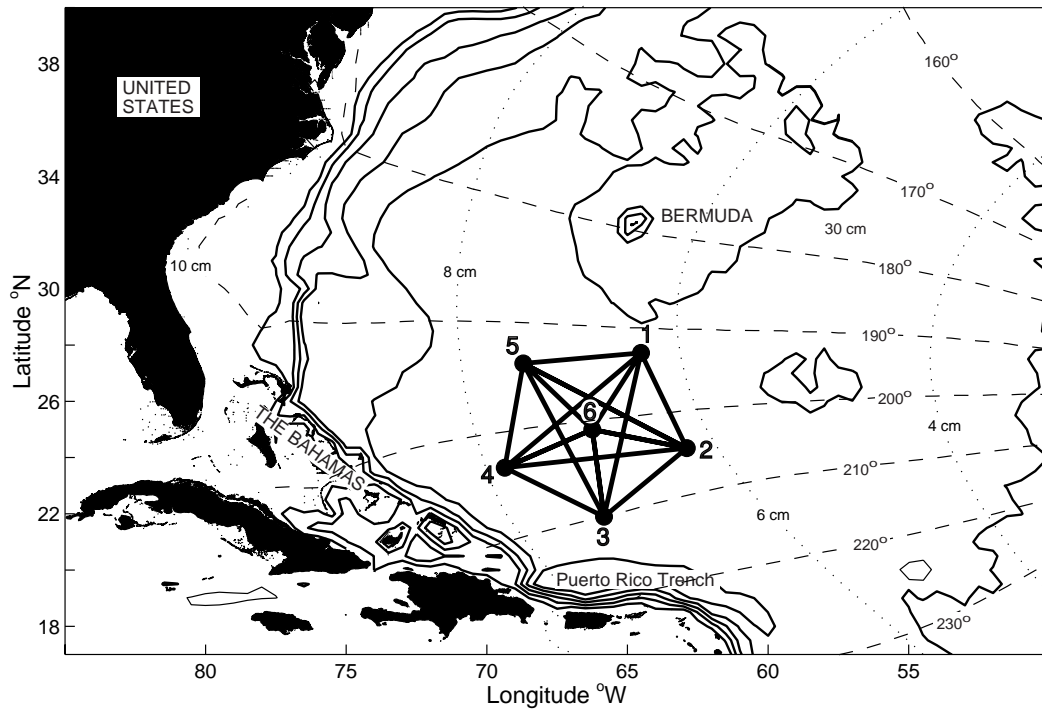


FIG. 8. The K_1 barotropic tidal elevation from the tidal model of Egbert et al. (1994) (TPXO.5 version). The dotted and dashed lines show the amplitude (in cm) and phase (in degrees), respectively. The phase of the diurnal tide changes by only about 20° along the Caribbean island arc.

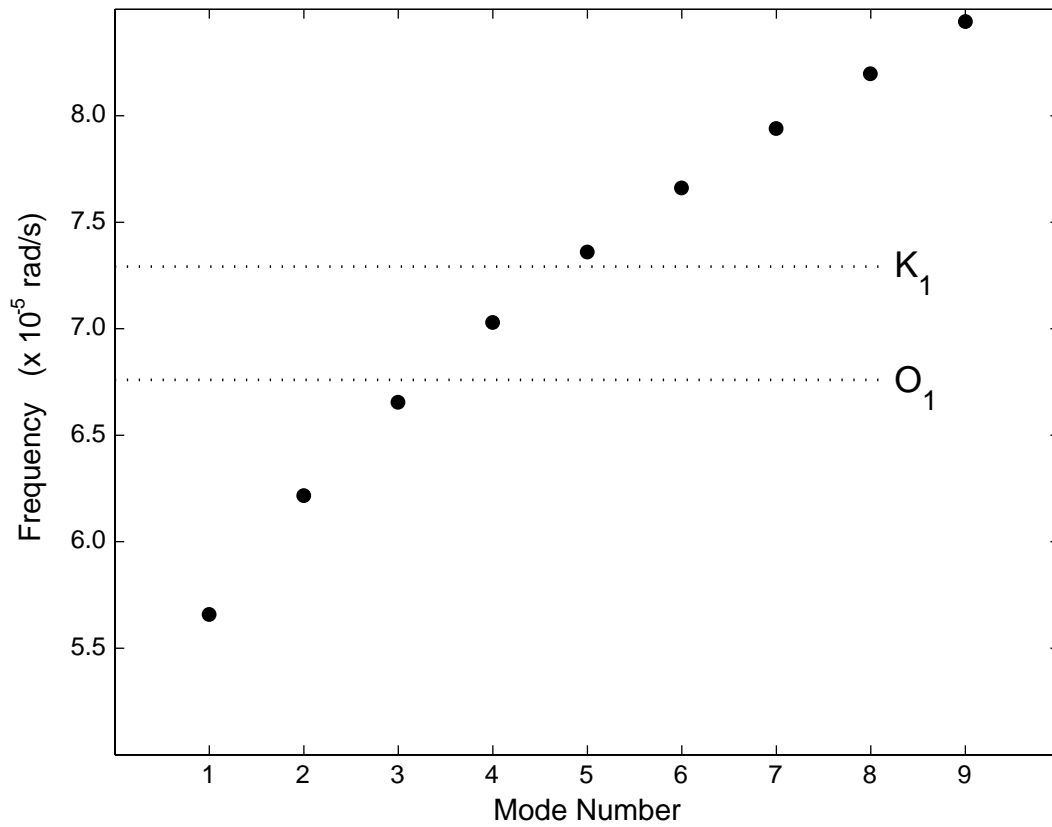


FIG. 9. Eigenfrequencies of (6) as a function of mode number determined by "shooting". The K_1 and O_1 frequencies are consistent with the eigenfrequencies, but the match is not exact.

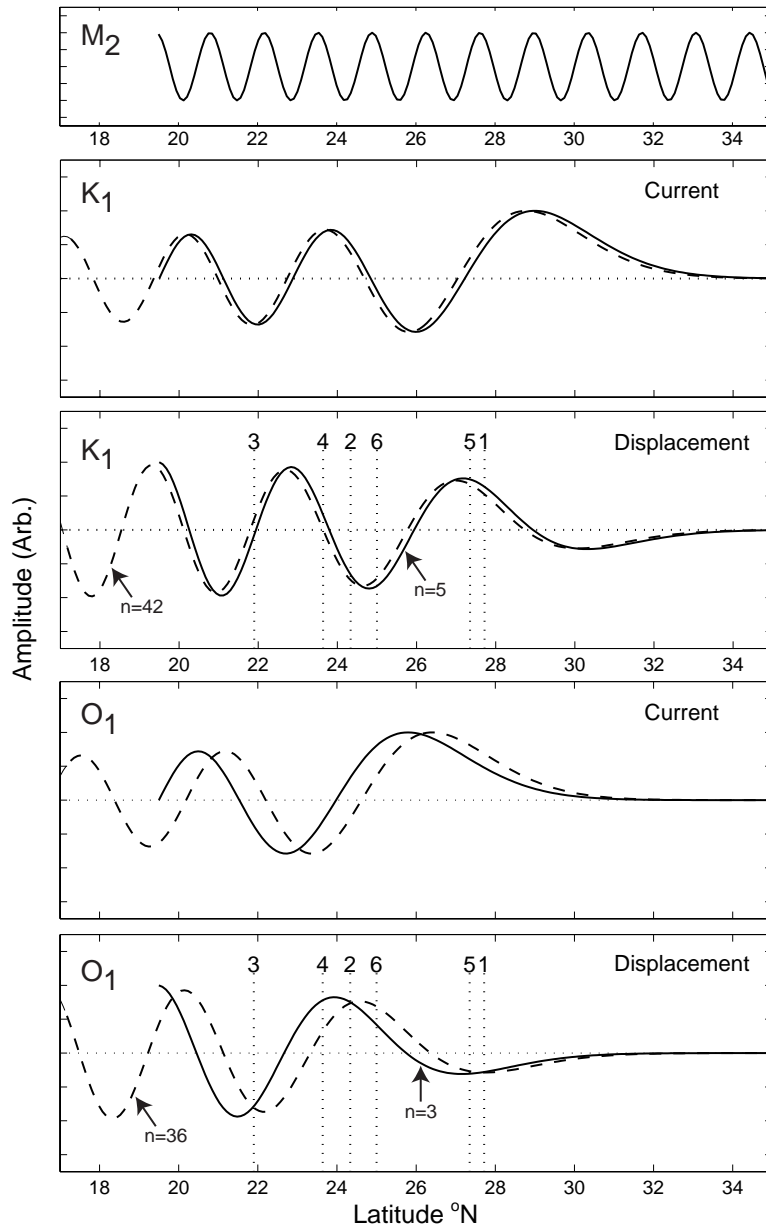


FIG. 10. Current and displacement modes as a function of latitude for the K_1 and O_1 constituents determined from the equatorial beta plane solutions (dashed; orders 42 and 36) and numerical solutions (solid; orders 5 and 3). The approximate and numerical solutions are similar and probably cannot be distinguished by the acoustic data. The locations of the 6 AMODE moorings are indicated in the panels for the displacement modes. A wave for semidiurnal frequencies (150-km wavelength) is shown in the top panel.

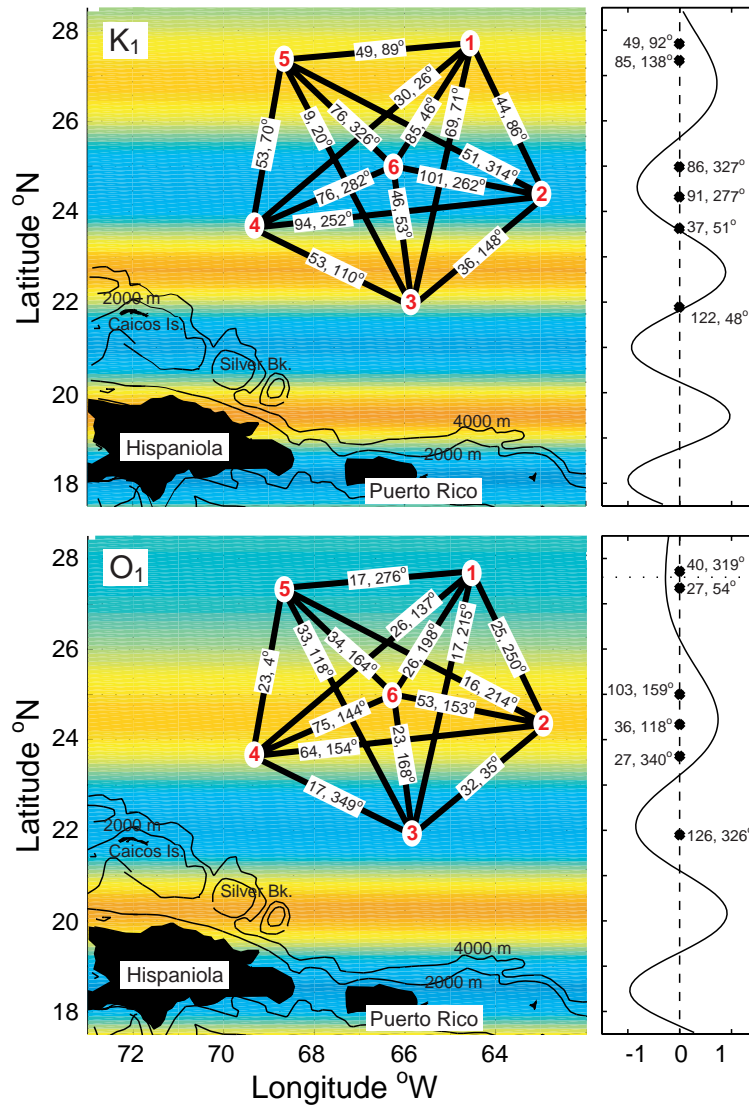


FIG. 11. The panels at left show the predicted displacement of diurnal waves at the K_1 and O_1 frequencies, together with the measured harmonic constants for each acoustic path. The panels at right show the predicted displacement as a function of latitude, together with the harmonic constants determined from the thermistor data obtained on each mooring. The horizontal dotted line in the panel for O_1 indicates the turning latitude. The boundary condition at 19–20 °N is zero meridional flow; which corresponds to maximum displacement. [From Dushaw and Worcester 1998.]

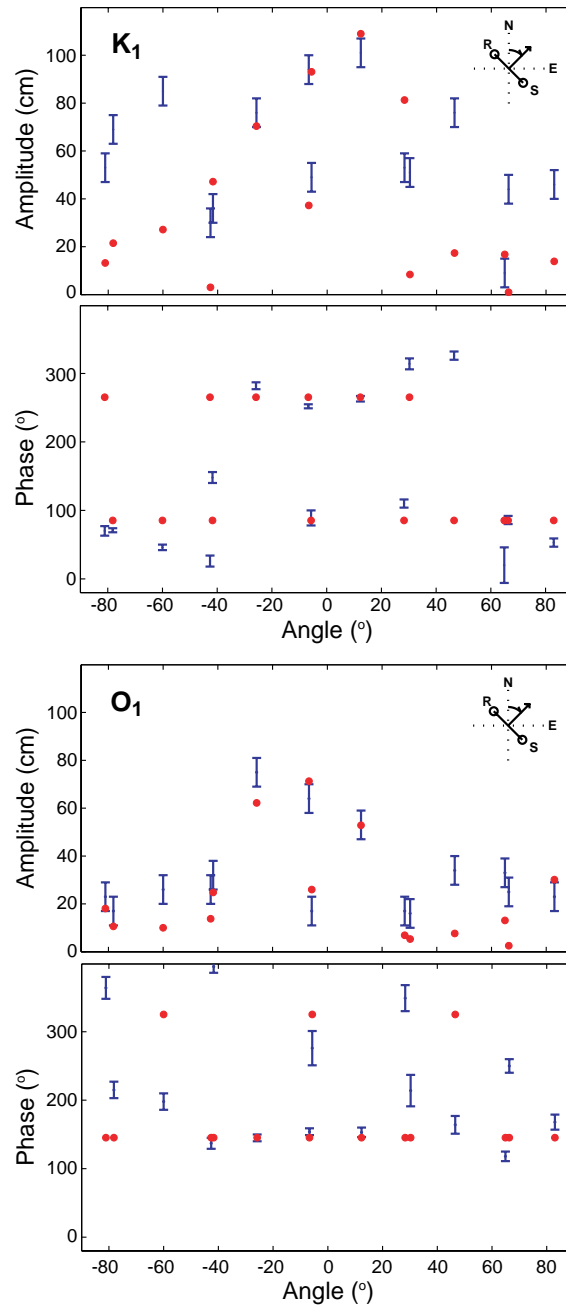


FIG. 12. Comparison of predicted resonant wave harmonic constants of the internal tide to measured harmonic constants (with error bars) for the (top) K_1 and (bottom) O_1 frequencies. For each comparison only two parameters (an amplitude and a phase) of the predicted wave are adjusted to fit to the 30 independent data. The harmonic constants are plotted as a function of the azimuthal angle of orientation of their acoustic path; zonal paths are at 0° .

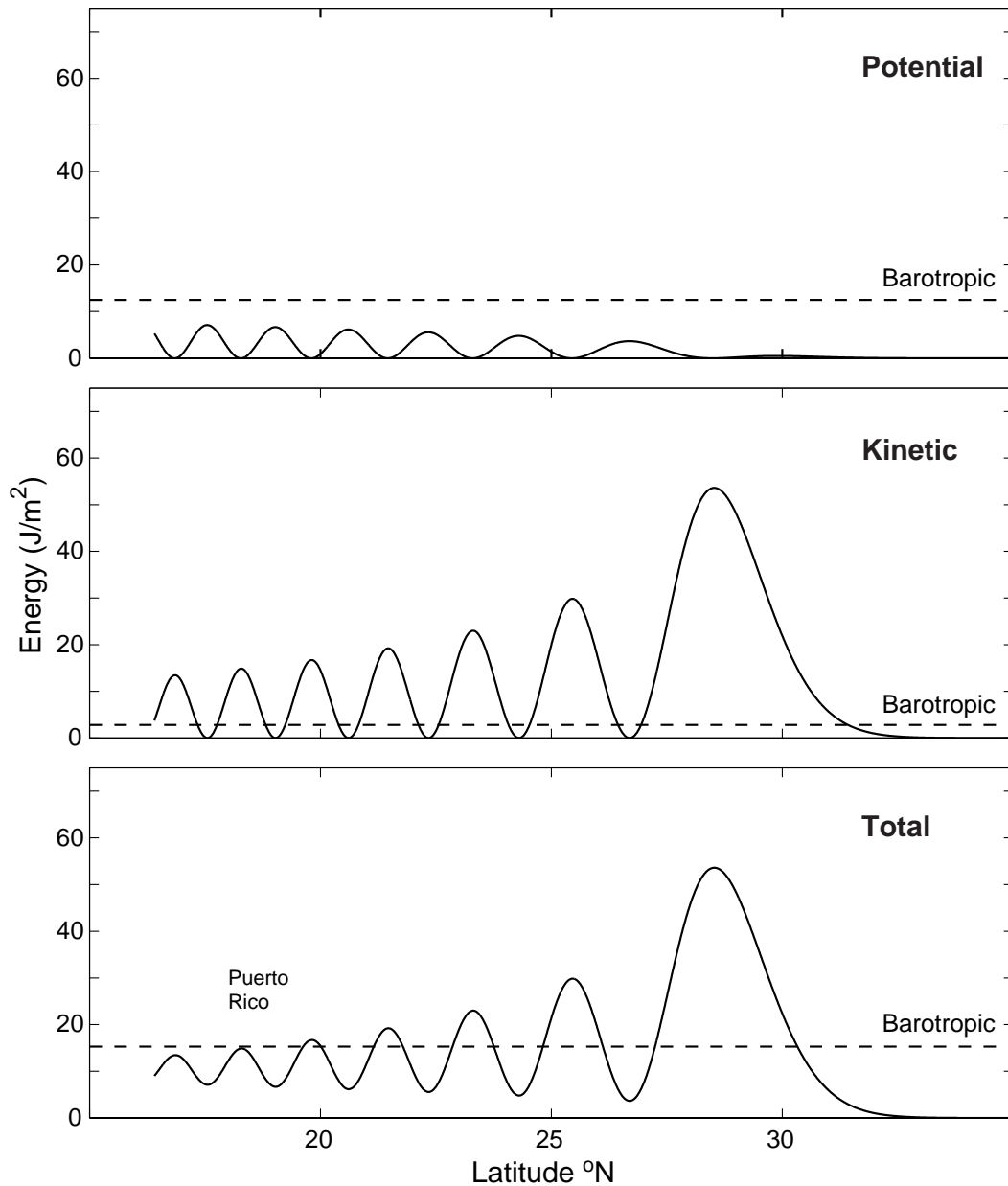


FIG. 13. Potential (top), kinetic (middle), and total energy of the K_1 internal tide as a function of latitude. The kinetic energy is inferred from the displacement. The barotropic energy is shown by the horizontal dashed line, showing that in some latitude bands the internal tide energy is many times larger than the barotropic energy for this frequency.

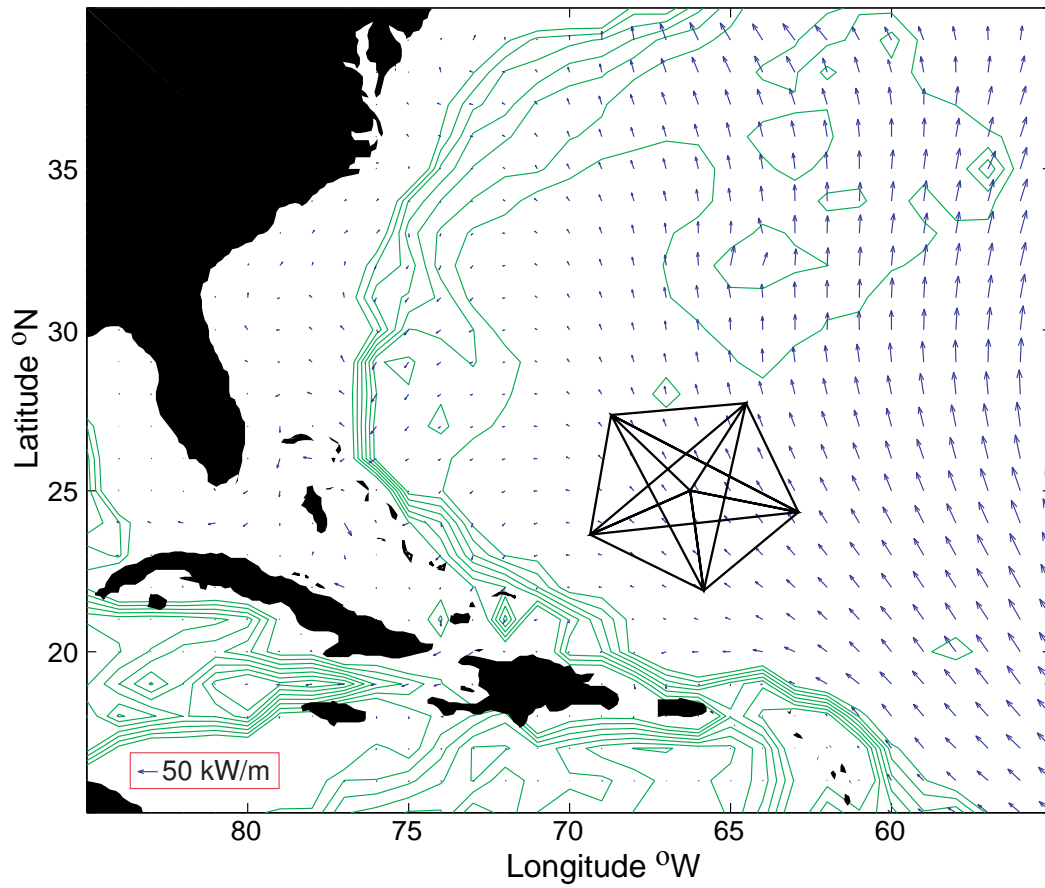


FIG. 14. M_2 barotropic tidal energy flux derived from the tidal model of Egbert et al. (1994) (TPXO.5 version). The tides are fairly large over the continental shelf of the United States; the lack of energy flux shows that the tide there is a standing wave.

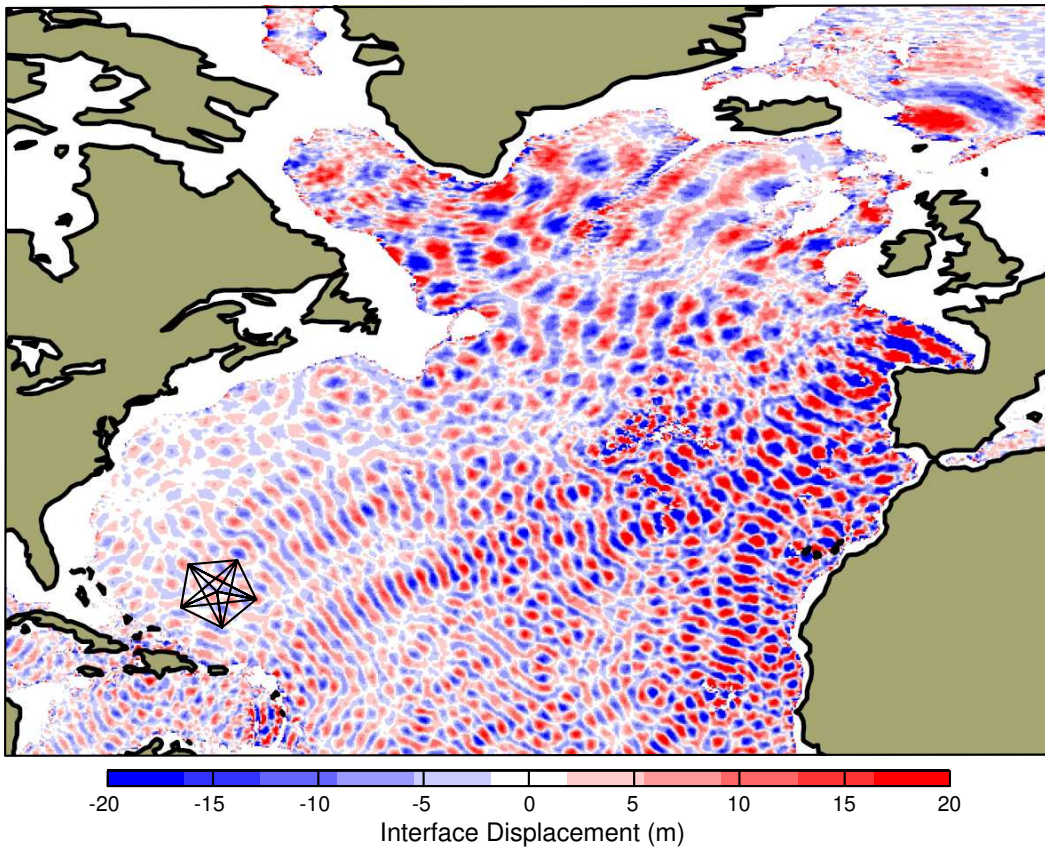


FIG. 15. The state of M_2 baroclinic tide radiation 20 days after the start of the Simmons et al. (2004) model run in the North Atlantic. According to this model, the M_2 internal tides are relatively weak in the AMODE region compared to other areas. Resonant M_2 internal tides are possibly evident east of Iceland, presumably trapped between topography and their 75°N turning latitude. Modified from Simmons et al. (2004).